



# A minimum albedo aerosol retrieval method for the new-generation geostationary meteorological satellite Himawari-8

Xing Yan<sup>a</sup>, Zhanqing Li<sup>a,b,\*</sup>, Nana Luo<sup>c</sup>, Wenzhong Shi<sup>d</sup>, Wenji Zhao<sup>e</sup>, Xingchuan Yang<sup>e</sup>, Jiannan Jin<sup>e</sup>

<sup>a</sup> State Key Laboratory of Earth Surface Processes and Resource Ecology, College of Global Change and Earth System Science, Beijing Normal University, Beijing, China

<sup>b</sup> Department of Atmospheric and Oceanic Science, Earth System Science Interdisciplinary Center, University of Maryland, College Park, MD, USA

<sup>c</sup> Department of Geography, San Diego State University, 5500 Campanile Dr., San Diego, CA 92182-4493, USA

<sup>d</sup> Department of Land Surveying and Geo-Informatics, The Hong Kong Polytechnic University, Hong Kong

<sup>e</sup> College of Resource Environment and Tourism, Capital Normal University, Beijing, China

## ARTICLE INFO

### Keywords:

Himawari-8  
Fine-mode fraction  
AOT  
Radiative transfer

## ABSTRACT

Aerosol properties, including aerosol optical thickness (AOT) and fine-mode fraction (FMF), are important physical data and are fundamental for climate studies. A minimum albedo aerosol retrieval method (MAARM) was developed for the retrieval of aerosol properties based on the new-generation geostationary meteorological satellite Himawari-8. This method is based on the albedo data which is directly obtained from the Himawari-8 and can successfully output AOT, FMF, and the Ångström exponent (AE) directly. As part of the MAARM, a modified radiative transfer equation was proposed that considers the impact of aerosol multiple scattering. Through comparisons with output from the Second Simulation of a Satellite Signal in the Solar Spectrum (6S) radiative transfer code, the modified radiative transfer equation achieved a high accuracy for the aerosol reflectance calculation (~5%). Aerosol Robotic Network (AERONET) data from three sites in Beijing and its surrounding area for the year 2016 were used to validate MAARM aerosol retrievals. Fifty-seven percent, 57%, and 56% of derived AOT values fell within the estimated error envelope at the Beijing, the Chinese Academy of Meteorological Sciences (CAMS), and Xianghe AERONET stations, respectively. In addition, 36% (58%) of MAARM-derived FMF values fell within the  $\pm 10\%$  AERONET FMF envelope (the  $\pm 25\%$  AERONET FMF envelope). Overall, an improvement was achieved by the MAARM in retrieving AOT, FMF, and AE compared with Himawari-8 standard aerosol property retrievals; however, there remains a distinct lack of skills in determining FMF and AE and their use from the MAARM retrieval is not recommended at this time. Given that the Himawari-8 satellite provides observations at 10-min intervals, the MAARM is capable of monitoring the spatial distribution of and variation in AOT with a high temporal resolution.

## 1. Introduction

Aerosols are known to have a substantial effect on the earth's energy balance and on climate change (Penner et al., 1992; Ramanathan et al., 2001). Most aerosols influence the climate through the scattering and absorption of solar radiation, and strongly absorbing aerosols may have a large impact on the hydrological cycle by warming the atmosphere (Ramanathan et al., 2007). Aerosols are also important because of their adverse effects on human health (Pope III et al., 2002) and air quality (Zaman et al., 2017; Liu et al., 2018). Anthropogenic aerosols can easily absorb some heavy metals and organic matter, and as a result, increase mortality rates and aggravate respiratory symptoms in exposed populations (Bell et al., 2007; Luo et al., 2016). Therefore, an assessment of

the effects of aerosols on the climate and human activities requires information regarding both the amount of aerosols present and the proportion of anthropogenic aerosols (Russell et al., 2010).

Jethva et al. (2014) showed that the fundamental aerosol parameter that primarily determines the strength and sign of radiative forcing is the aerosol optical thickness (AOT). The AOT is a measure of the wavelength-dependent aerosol extinction in the atmospheric column. For anthropogenic aerosols, Bellouin et al. (2005) reported that the fine-mode fraction (FMF) can be used to separate man-made aerosols from natural ones, and that anthropogenic aerosols are associated with FMFs larger than  $0.83 \pm 0.05$  while natural aerosols are associated with FMFs smaller than  $0.35 \pm 0.05$ . Thus, an accurate estimation of these aerosol properties is fundamental for climate studies and the evaluation

\* Corresponding author at: ESPRE/GCESS, Beijing Normal University, 19 Xijiekouwai Street, Haidian District, Beijing 100875, China.  
E-mail address: [zli@atmos.umd.edu](mailto:zli@atmos.umd.edu) (Z. Li).

of anthropogenic impacts.

There are currently two common ways to obtain data regarding aerosol properties: one way is to make ground-based measurements such as what is done by the Aerosol Robotic Network (AERONET) and the other way is to make spaceborne observations. The AERONET is a globally distributed network of Sun photometers that measures directly transmitted solar radiation during daylight hours (Holben et al., 1998). Many studies have shown that AERONET can provide highly accurate aerosol property data. The uncertainty for AOT is 0.01–0.02 (Eck et al., 1999) and 0.1 for the FMF (O'Neill et al., 2001b, 2003). However, AERONET is based on point measurements and has a much smaller spatial coverage than do satellites.

Space-based remote sensing techniques for measuring aerosol properties have been developed (Alvim et al., 2017; Sun et al., 2017). Satellites provide information regarding the spatial distribution of aerosols from regional to global scales. Several satellites have successfully recorded official aerosol property data. The Moderate Resolution Imaging Spectroradiometer (MODIS) is considered to be effective in obtaining AOT information and the MODIS Atmosphere Level 2 aerosol product has also been widely used (Remer et al., 2005). It has three aerosol retrieval algorithms: the Dark Target (DT) land algorithm, the DT ocean algorithm, and the Deep Blue (DB) algorithm. AOT, FMF, and Ångström exponent (AE) data can be extracted from the MODIS aerosol product. Only the DT algorithm provides FMF outputs. However, the MODIS FMF is unreliable over land, as has been shown in many studies (Bellouin et al., 2005; Levy et al., 2007, 2010). To overcome this limitation, Yan et al. (2017) proposed a look-up table (LUT) spectral deconvolution algorithm (LUT-SDA) method for the FMF retrieval, which has been successfully applied to MODIS data.

In recent years, due to rapid urbanization all over the world, especially in Asia, haze has become a serious problem in many countries. The DT algorithm underestimates haze aerosol loading (Tao et al., 2012). One reason is that the aerosol model on hazy days is different from that on less polluted days so the default aerosol model in the DT land algorithm of MODIS AOT products may not be suitable (Yan et al., 2016). The information required to model aerosol properties is best obtained from ground based observation. But in many developing countries, there are a limited number of ground-based aerosol monitoring stations. Bilal et al. (2013) developed a Simplified high-resolution Aerosol Retrieval Algorithm for MODIS data that does not use aerosol model information as input and assumes that the aerosol reflectance is calculated using a single scattering approximation. However, Antoine and Morel (1998) reported that notable differences exist between single scattering and multiple scattering approximations for aerosols in the visible spectrum.

In addition to MODIS, the Ozone Monitoring Instrument, the Advanced Along-Track Scanning Radiometer, the Suomi National Polar-orbiting Partnership Visible Infrared Imaging Radiometer Suite, and the Multi-angle Imaging Spectroradiometer can also provide aerosol data (Ahn et al., 2008; Huang et al., 2016; Kahn et al., 2010; Patadia et al., 2013; Rodríguez et al., 2015; Torres et al., 2007). However, the temporal resolution of these satellites is low (one observation per day) so they cannot be used to determine hourly aerosol property variability.

Himawari-8, Japan's new-generation geostationary meteorological satellite (Bessho et al., 2016), was launched on 7 October 2014 and entered operational service on 7 July 2015 at 140°E, covering East Asia and the Western Pacific Region (Sekiyama et al., 2016). The Advanced Himawari Imager onboard Himawari-8 has 3 spectral bands in the visible, 3 bands in the near-infrared and shortwave-infrared, and 10 bands in the thermal-infrared (Murakami, 2016). Himawari-8 has a high temporal resolution (10 min) and can provide multiple observations for a single location, which makes it suitable for monitoring aerosol variations.

We propose an algorithm called the minimum albedo aerosol retrieval method (MAARM) to retrieve aerosol properties using data from the Himawari-8 satellite. The method that we have developed integrates a modified radiative transfer equation and the LUT-SDA, and can output AOT, FMF and AE directly. In addition, the proposed algorithm includes the following features: (1) it considers the impact of multiple scattering for aerosols and is computationally efficient, and (2) this algorithm uses the Himawari-8 albedo data to calculate surface reflectance, in contrast with other methods that use the MODIS surface reflectance product (MOD09) as input (Bilal et al., 2013; Li et al., 2013; Sun et al., 2015; Wu et al., 2016). The only data source for the retrieval of aerosol properties is Himawari-8 measurements. The retrieved AOT, FMF, and AE were compared with AERONET retrievals and the current Himawari-8 official product over Beijing and its surrounding area. Owing to the ability of the Himawari-8 satellite to provide observations at 10-min intervals, this improved algorithm has the potential to monitor the spatial distribution of and variation in aerosol properties at a high temporal resolution.

## 2. Data and methods

### 2.1. Himawari-8 satellite data

Daytime (0310 coordinated universal time, or 0310 UTC) Himawari L1 Gridded Data with a spatial resolution of 5 km were acquired from 1 January to 31 December 2016 (<http://www.eorc.jaxa.jp/ptree>). Himawari L1 Gridded Data provides the albedo (Bands 1 to 6) and brightness temperature (Bands 7 to 16) at a 10-min temporal resolution. In this study, we used Band 1 (blue, 0.47  $\mu\text{m}$ ) and Band 3 (red, 0.64  $\mu\text{m}$ ) data to retrieve aerosol properties. Level 2 Aerosol Property parameters (Version 1.0) with the same spatial (5 km) and temporal resolutions (10-min) as Himawari L1 Gridded Data were extracted from the Himawari-8 Geophysical Parameter dataset for comparison purposes. These parameters include AOT at 500 nm and AE, which are based on the retrieval algorithms of Fukuda et al. (2013) over land and Higurashi and Nakajima (1999, 2002) over oceans, and the FMF, i.e., the “Optical Depth Ratio (fine)” variable in the Himawari-8 Geophysical Parameter dataset.

### 2.2. MODIS C6 MOD04 product

MODIS Collection 6 (C6) aerosol products (MOD04) were obtained and C6 DT algorithm-based AOT (variable name: Optical\_Depth\_Land\_And\_Ocean) and FMF (variable name: Optical\_Depth\_Ratio\_Small\_Land) were used for comparisons with MAARM retrievals and Himawari-8 official aerosol data. In addition, MODIS C6 DB AOT at a 10-km resolution (variable name: Deep\_Blue\_Aerosol\_Optical\_Depth\_550\_land\_Best\_Estimate) was also obtained for comparison purposes and filtered using quality assurance (QA) information (Hsu et al., 2013; Sayer et al., 2013).

We selected the 10-km resolution MODIS C6 AOT product due to its higher accuracy relative to the 3-km resolution AOT product (Munchak et al., 2013; Yan et al., 2016). The C6 DT AOT product uses the VISvs2.1 surface reflectance parameterization with a shortwave-infrared normalized difference vegetation index dependence (Levy et al., 2013), which is described by Levy et al. (2007).

### 2.3. AERONET

The AERONET is a globally distributed network, which provides multi-wavelength AOT measurements with a high accuracy and an uncertainty < 0.02 (Holben et al., 2001). Standard AERONET AOT products were acquired in bands centered at 340, 380, 440, 500, 675,

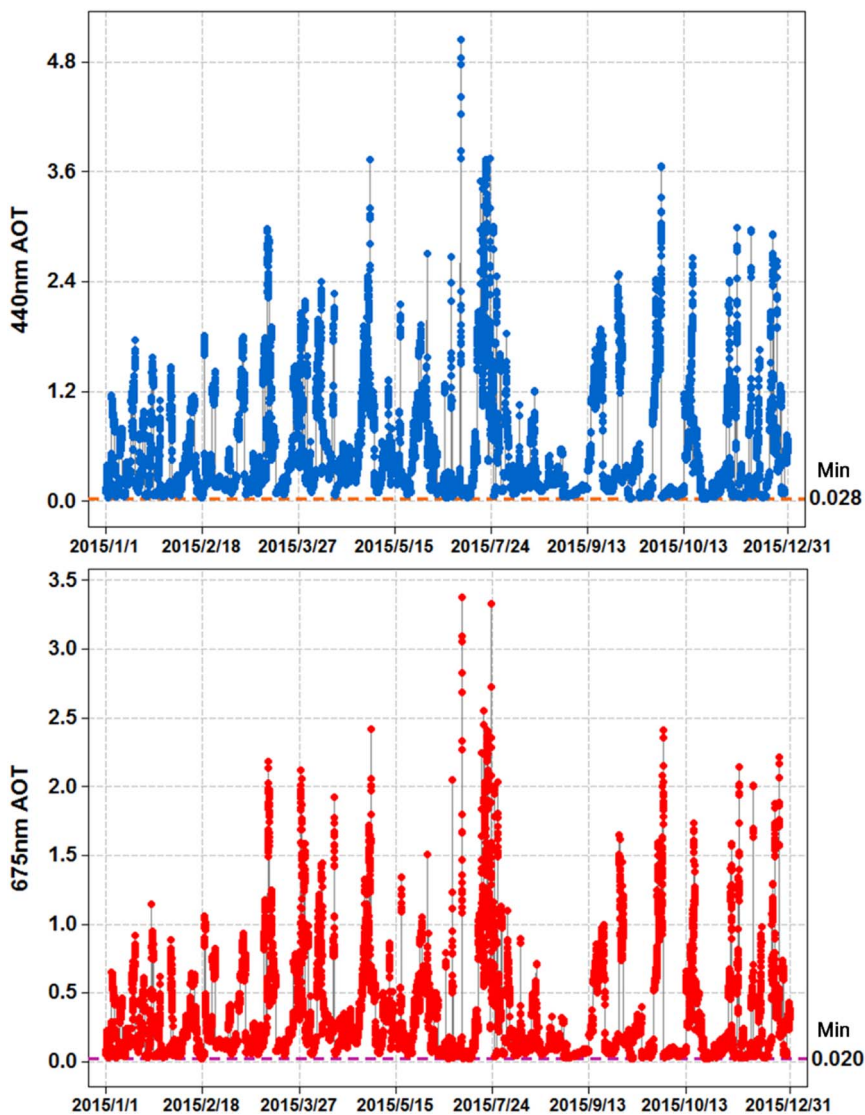


Fig. 1. Time series plots of AERONET Level 2.0 AOT at 440 and 675 nm at the CAMS site. Data are from 2015.

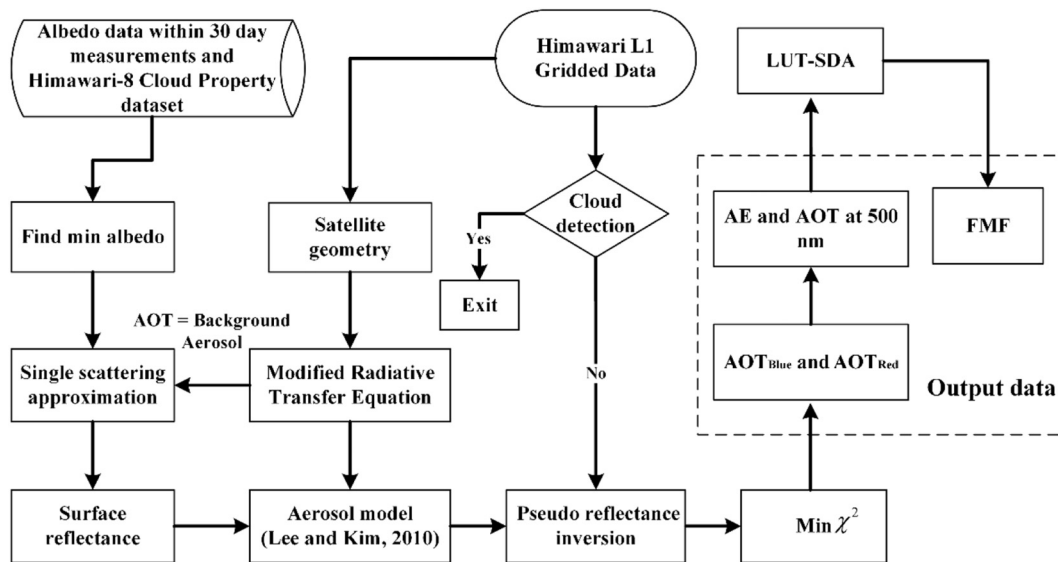


Fig. 2. Flowchart describing the MAARM.

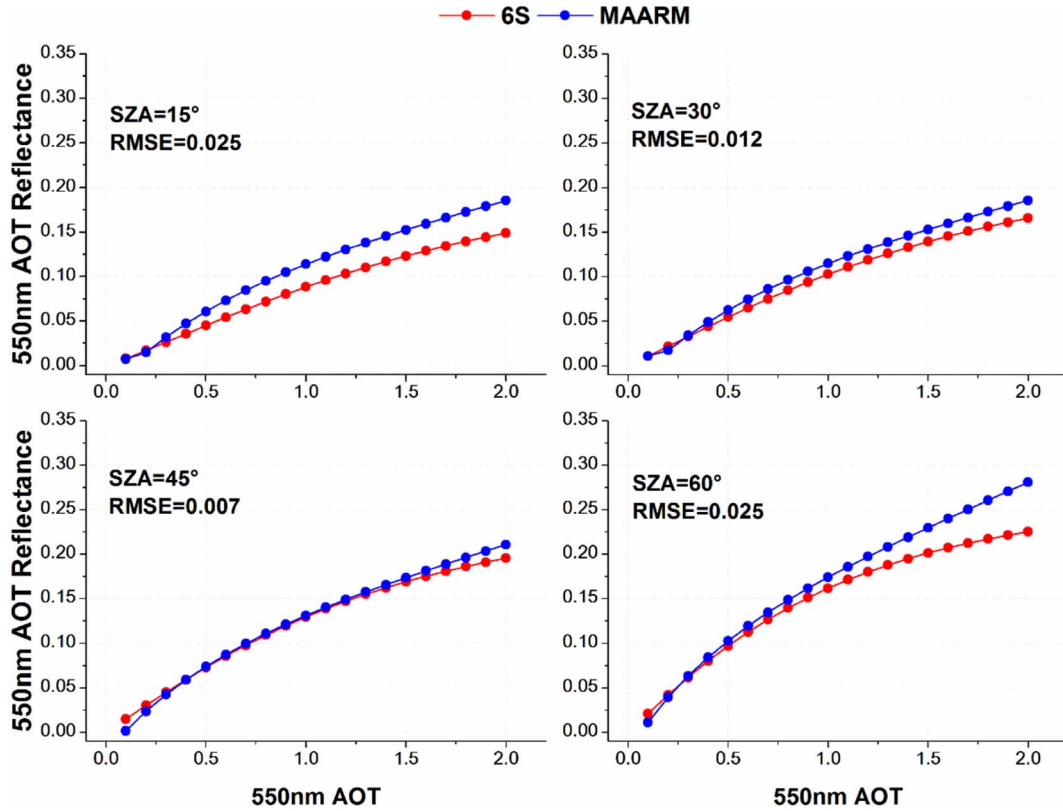


Fig. 3. Aerosol reflectance as a function of AOT at 550 nm for four solar zenith angles (SZAs). 6S and MAARM results are shown in red and blue, respectively. Root-mean-square errors are given. The satellite azimuth angle is 145°, satellite zenith angle is 53° and solar azimuth angle is 155°. (For interpretation of the references to color in this figure legend, the reader is referred to the web version of this article).

870, and 1020 nm at three sites: Beijing (39.98°N, 116.38°E), the Chinese Academy of Meteorological Sciences (CAMS; 39.93°N, 116.32°E), and XiangHe (39.75°N, 116.96°E). Version 2 AERONET products were also used, including Level 2.0 AOT and Level 2.0 spectral de-convolution algorithm (SDA). The locations of the sites are shown in Fig. S1. Level 2.0 data are subject to full quality control, including cloud screening and before-and-after radiometric calibration (Smirnov et al., 2000).

#### 2.4. Modified radiative transfer equation

First, as assumed in the Second Simulation of the Satellite Signal in the Solar Spectrum (6S) radiative transfer algorithm, the surface reflectance is considered to be Lambertian in this study (Vermote et al., 2006). For the assumption of Lambertian, Li et al. (2013) indicated that the majority of the North China Plain has an elevation of < 50 m above sea level, which has a weak surface BRDF effect compared to more complex terrains. The albedos for Band 1 (blue, 0.47 μm) and Band 3 (red, 0.64 μm) were extracted from Himawari L1 Gridded Data and are defined as:

$$\text{albedo} = \rho^* \times \cos(\theta_0), \quad (1)$$

where  $\theta_0$  is the solar zenith angle and  $\rho^*$  is the top-of-the-atmosphere reflectance observed by the satellite.

The satellite-measured reflectance can be estimated as (Drury et al., 2008):

$$\rho^* = \rho^a + \frac{T_{(\theta_0)}T_{(\theta)}}{1 - \rho_s S_{(\lambda)}} \rho_s, \quad (2)$$

where  $\theta$  is the satellite zenith angle,  $\rho^a$  is the atmospheric reflectance,  $\rho_s$  is the surface reflectance,  $T_{(\theta_0)}$  and  $T_{(\theta)}$  are the downward and upward total scattering transmittances, respectively, and  $S_{(\lambda)}$  is the atmospheric backscattering ratio.

The variable  $\rho^a$  can be expressed as the sum of the aerosol reflectance  $\rho_{Aer}$  and Rayleigh reflectance  $\rho_{Ray}$  for molecules:

$$\rho^a = \rho_{Aer} + \rho_{Ray}. \quad (3)$$

The variable  $\rho_{Aer}$  is the aerosol reflectance in the absence of air molecules. In this study, we assume that  $\rho_{Aer}$  is composed of two parts:

$$\rho_{Aer} = R^I + R^{II}, \quad (4)$$

where  $R^I$  accounts for single scattering and  $R^{II}$  is the contribution made by multiple scattering.

The single scattering approximation  $R^I$  is calculated as (Antoine and Morel, 1998):

$$R^I(\mu, \mu_0, \phi - \phi_0) = \frac{\omega_0 \tau_a P_a(\mu, \mu_0, \phi - \phi_0)}{4\mu_0\mu}, \quad (5)$$

where  $\mu_0$  is the cosine of the solar zenith angle,  $\mu$  is the cosine of the sensor zenith angle,  $\phi - \phi_0$  is the relative azimuth between the viewing angle  $\phi$  and the solar direction  $\phi_0$ ,  $\tau_a$  is the AOT,  $\omega_0$  is the single scattering albedo (SSA), and  $P_a(\mu, \mu_0, \phi - \phi_0)$  is the aerosol scattering phase function.

Multiple scattering represented by  $R^{II}$  is approximated by the second-order scattering equation (Hansen and Travis, 1974):

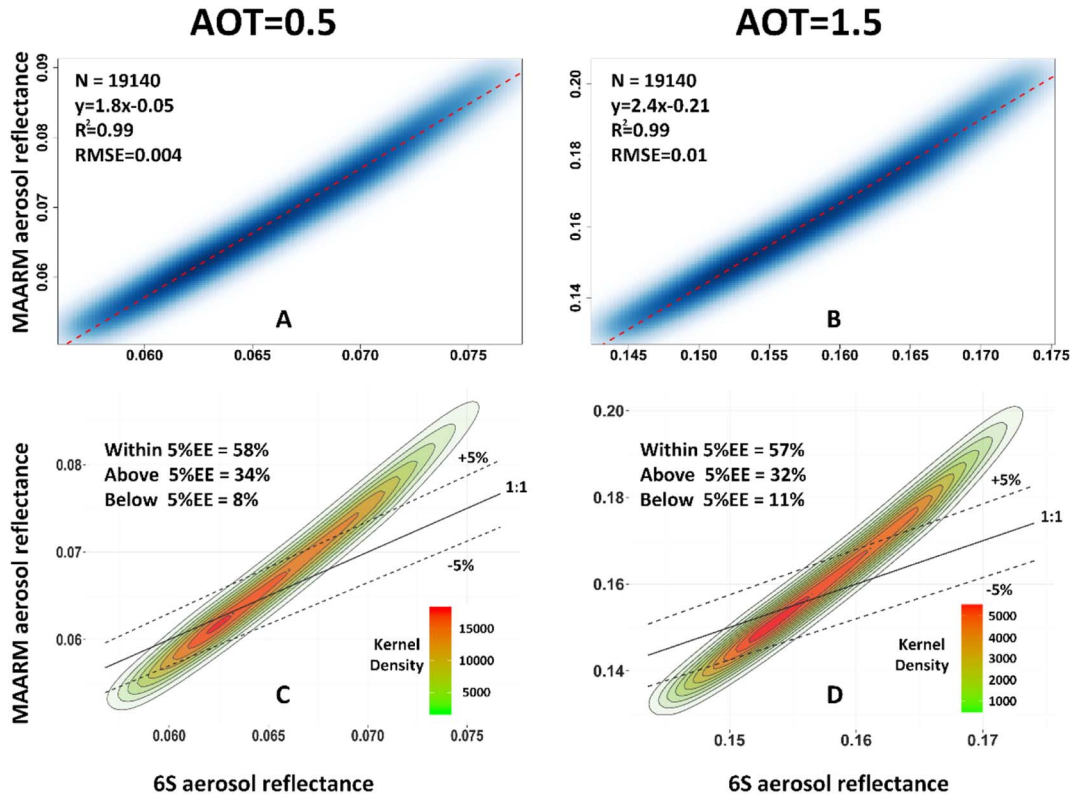


**Fig. 4.** MAARM-derived aerosol reflectance as a function of 6S-derived aerosol reflectance when (A and C) AOT (550 nm) = 0.5 and (B and D) AOT (550 nm) = 1.5. Himawari-8 viewing geometry parameters are used. Red dotted lines show the best-fit lines from linear regression. The regression equations and coefficients of determination ( $R^2$ ) are given as well as the number of data points (N) and the root-mean-square errors (RMSE). Panels (C) and (D) show the corresponding kernel density values (shaded colored ovals). The solid black lines are the 1:1 lines from (A) and (B) and the dotted black lines are the estimated error (EE) envelope lines, which are equal to  $\pm 5\% \times 6S$  aerosol reflectance. (For interpretation of the references to color in this figure legend, the reader is referred to the web version of this article).

$$\begin{aligned}
 \left(\frac{1}{\mu} + \frac{1}{\mu_0}\right) R_{11}(\mu, \mu_0, \phi - \phi_0) &= \frac{\omega_0}{4\pi\mu} \int_0^{2\pi} \int_0^1 P_1(\mu, \mu', \phi - \phi') R_1(\mu', \mu_0, \phi' - \phi_0) d\mu' d\phi' \\
 &+ \frac{\omega_0}{4\pi\mu_0} \int_0^{2\pi} \int_0^1 R_1(\mu, \mu', \phi - \phi') P_1(\mu', \mu_0, \phi' - \phi_0) d\mu' d\phi' \\
 &- \frac{\omega_0 e^{-\tau_a}}{4\pi\mu_0} \int_0^{2\pi} \int_0^1 T_1(\mu, \mu', \phi - \phi') P_r(\mu', \mu_0, \phi' - \phi_0) d\mu' d\phi' \\
 &- \frac{\omega_0 e^{-\tau_a}}{4\pi\mu} \int_0^{2\pi} \int_0^1 P_r(\mu, \mu', \phi - \phi') T_1(\mu', \mu_0, \phi' - \phi_0) d\mu' d\phi',
 \end{aligned} \quad (6)$$

where  $R_1$  is the first-order scattering of aerosols (Hansen and Travis, 1974):

$$R_1(\mu, \mu_0, \phi - \phi_0) = \frac{\omega_0 P_r(\mu, \mu_0, \phi - \phi_0)}{4(\mu_0 + \mu)} \left\{ 1 - \exp \left[ -\tau_a \left( \frac{1}{\mu} + \frac{1}{\mu_0} \right) \right] \right\}. \quad (7)$$

In this study, only the first- and second-order scattering by aerosols are accounted for in the aerosol multiple scattering approximation, and it neglects terms proportional to the power of 2 and higher of the aerosol optical thickness.  $P_r$  is the modified Henyey-Greenstein function, which is a function that moderates the overall contributions in forward and backward scattering and is defined as (Rahman et al., 1993):

$$P_r(\mu, \mu_0, \phi - \phi_0) = \frac{1 - g^2}{[1 + g^2 - 2g \cos(\pi - \xi)]^{1.5}}, \quad (8)$$

where  $g$  is the asymmetry factor. The phase angle  $\xi$  is given by:

$$\begin{aligned}
 \cos(\xi) &= \cos(\theta_0) \cos(\theta) + \sin(\theta_0) \sin(\theta) \cos(\phi - \phi_0) \\
 &= \mu_0 \mu + \sqrt{(1 - \mu_0^2)(1 - \mu^2)} \cos(\phi - \phi_0).
 \end{aligned} \quad (9)$$

$P_t$  is the Henyey-Greenstein phase function, which depends on the scattering angle  $\Theta_t$ .  $T_1$  is the single scattering transmittance given by (Seidel et al., 2012):

$$T_1(\mu, \mu_0, \phi - \phi_0) = \frac{\omega_0 P_t(\Theta_t)}{4(\mu - \mu_0)} \left[ \exp\left(\frac{-\tau_a}{\mu}\right) - \exp\left(\frac{-\tau_a}{\mu_0}\right) \right]. \quad (10)$$

From l'Hospital's rule, for  $\mu = \mu_0$ ,

$$T_1(\mu_0, \mu_0, \phi - \phi_0) = \frac{\omega_0 \tau_a}{4\mu_0^2} \exp\left(\frac{-\tau_a}{\mu_0}\right) P_t(\Theta_t). \quad (11)$$

Then the Rayleigh reflectance for molecules  $\rho_{Ray}(\mu, \mu_0, \phi - \phi_0)$  can be approximated by (Antoine and Morel, 1998):

$$\rho_{Ray}(\mu, \mu_0, \phi - \phi_0) = \frac{\omega_R \tau_R P_R(\mu, \mu_0, \phi - \phi_0)}{4\mu_0 \mu}, \quad (12)$$

where  $\tau_R$  is the Rayleigh optical depth,  $P_R(\mu, \mu_0, \phi - \phi_0)$  is the Rayleigh scattering phase function, and  $\omega_R$  is the Rayleigh single-scattering albedo. In this study,  $\omega_R \approx 1$ .

$T_{(\theta_0)}$  and  $T_{(\theta)}$  are defined by (Vermote et al., 2006):

$$\begin{aligned}
 T_{(\theta_0)} &= \exp \left[ \frac{-(\tau_R + \tau_a)}{\mu_s} \right] + t_d(\mu_s) \\
 T_{(\theta)} &= \exp \left[ \frac{-(\tau_R + \tau_a)}{\mu_v} \right] + t_d(\mu_v)
 \end{aligned} \quad (13)$$

In this study,  $t_d(\mu_s)$  and  $t_d(\mu_v)$  are identical (Vermote et al., 2006). The diffuse transmittance  $t_d(\mu)$  is then approximated by (Liu and Liu, 2009; Tanre et al., 1979):

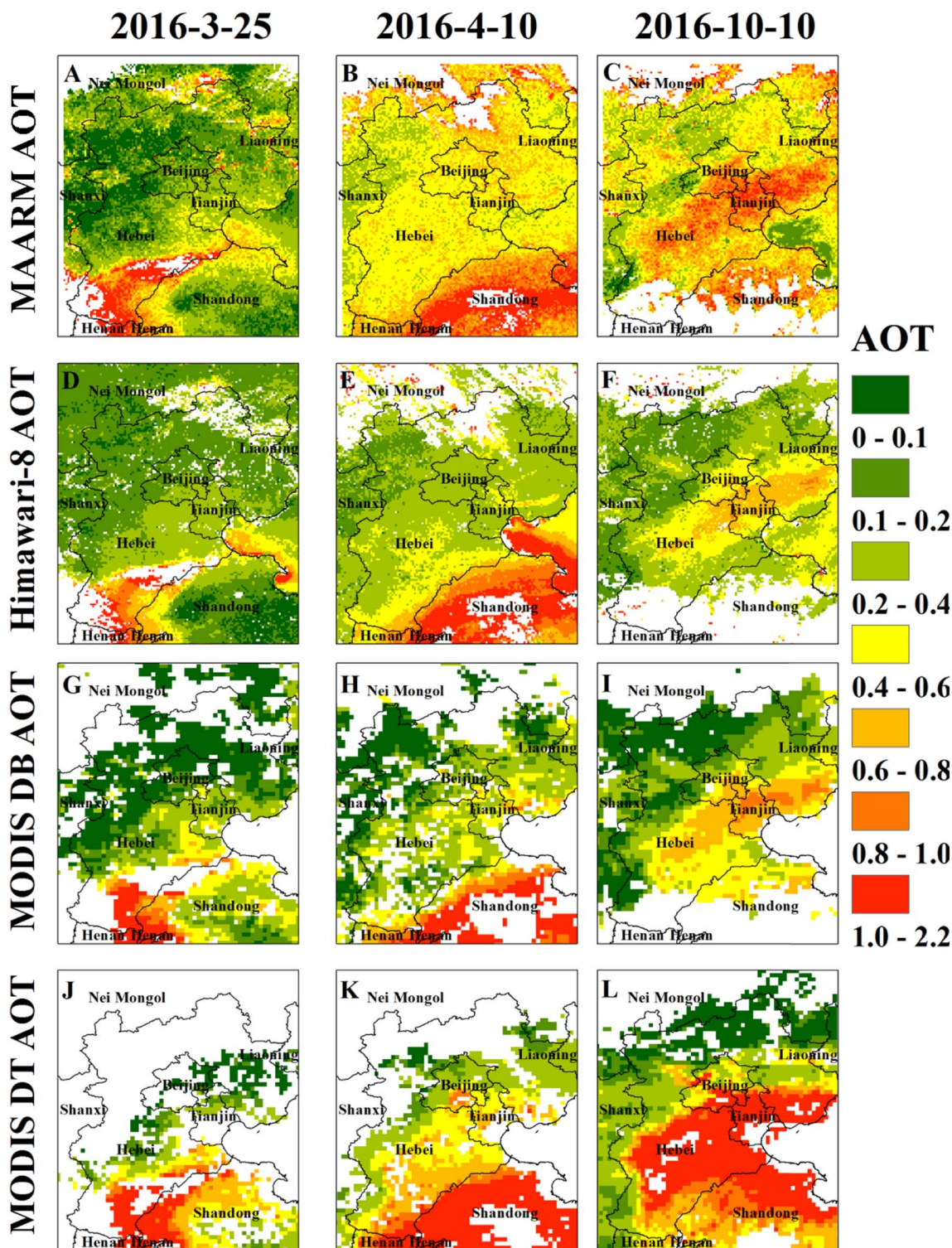


Fig. 5. Spatial distributions of AOT retrieved from the MAARM (A–C), Himawari-8 (D–F), the MODIS DB algorithm (G–I), and the MODIS DT algorithm (J–L) on three days: 25 March 2016 (leftmost column), 10 April 2016 (middle column), and 10 October 2016 (rightmost column). All of the satellite images are acquired at 0310 coordinated universal time. MAARM and Himawari-8 retrievals are AOT at 500 nm and MODIS DT and DB retrievals are AOT at 550 nm.

$$t_a(\mu) = \exp(-(\tau_R + \tau_a)/\mu)\{\exp[(0.52\tau_R + \tau_a(1 + g)/2)/\mu] - 1\}. \quad (14)$$

### 2.5. MAARM

Other parameters used in this study can be found in the Supplementary material. Note that  $T_{(\omega_0)}$  and  $T_{(\omega)}$  used in this study are different from those used by Bilal et al. (2013). Bilal et al. (2013) omitted the diffuse transmittance for simplification. This difference is also shown in the Supplementary material.

Himawari L1 Gridded Data includes the gas absorption correction developed by Levy et al. (2009). We assume that the minimum albedo within 30 days has the lowest aerosol impact and is only influenced by background aerosols ( $\tau_B$ ). The minimum albedo is obtained from Himawari L1 Gridded Data, and the cloud is masked by Himawari-8 Cloud

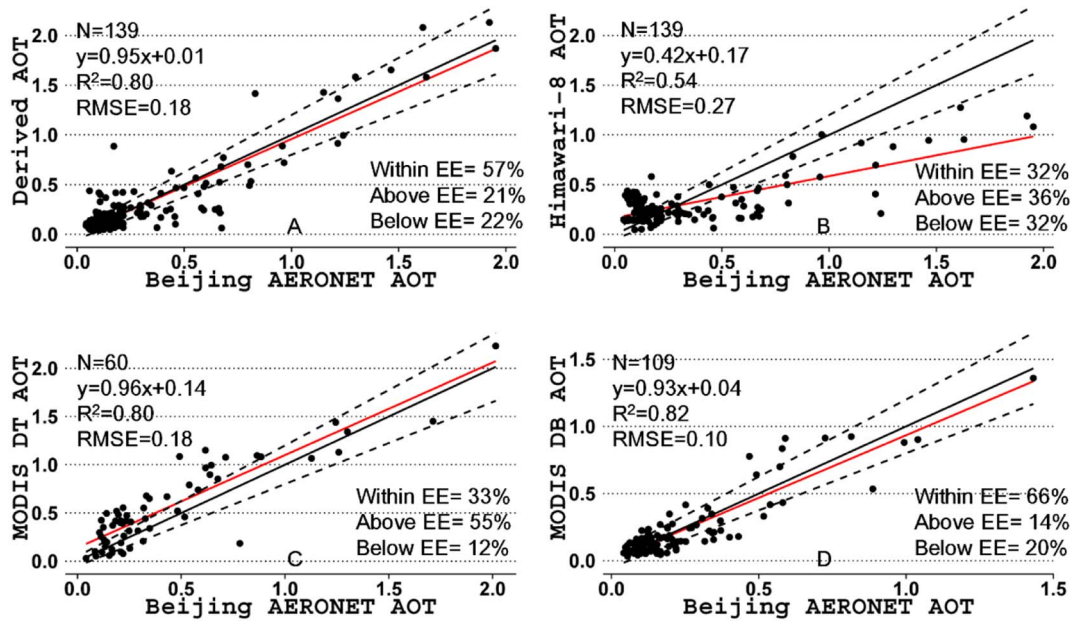


Fig. 6. (A) MAARM, (B) Himawari-8, (C) MODIS DT, and (D) MODIS DB AOT retrievals as a function of AERONET AOT at the Beijing site. The red lines are the best-fit lines from linear regression and the black solid lines are the 1:1 lines. The two dashed error lines are  $y = 1.15x + 0.05$  (upper line) and  $y = 0.85x - 0.05$  (bottom line), which correspond to the error  $\Delta\tau = \pm (0.05 + 0.15A_{ERONET\ AOT})$ . The regression equations and coefficients of determination ( $R^2$ ) are given as well as the number of data points (N) and the root-mean-square errors (RMSE). (For interpretation of the references to color in this figure legend, the reader is referred to the web version of this article).

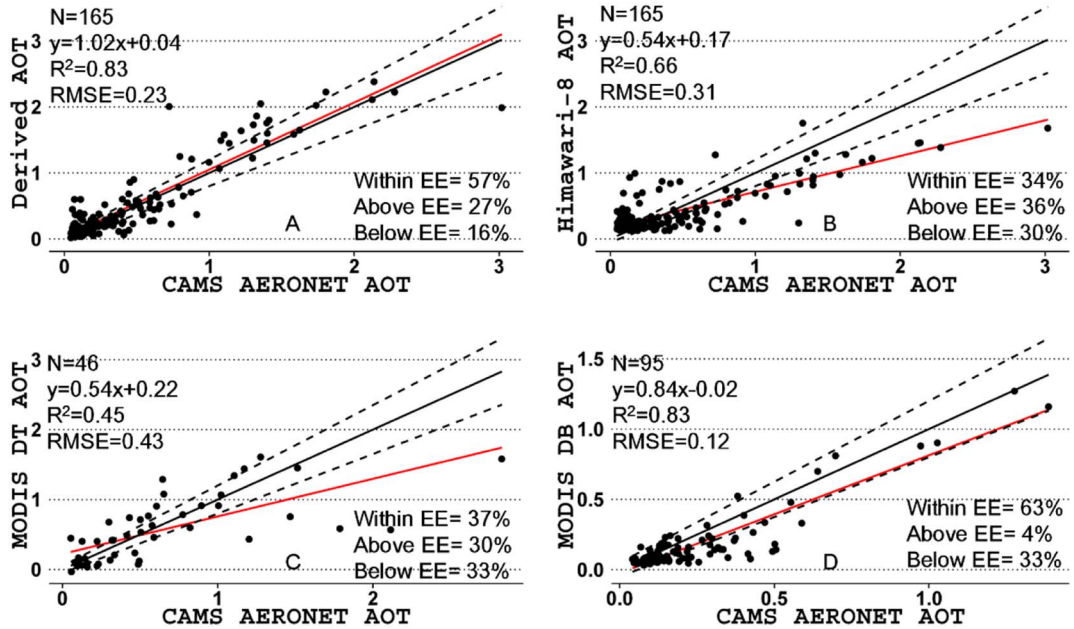


Fig. 7. Same as Fig. 6 but for the CAMS site.

Property dataset, only the cloud free pixel will be as the candidate for the minimum albedo selection. Thus  $\rho^*$  is expressed as:

$$\rho^* = \rho_{Ray} + \rho_{Aer}(\tau_a = \tau_B) + \frac{T_{(\theta_0, \tau_a = \tau_B)} T_{(\theta, \tau_a = \tau_B)} \rho_s}{1 - \rho_s S_{(\lambda, \tau_a = \tau_B)}} \quad (15)$$

Then  $\rho_s$  can be derived using the following expression:

$$\begin{aligned} \rho_s &= \frac{\rho^* - \rho_{Ray} - \rho_{Aer}(\tau_a = \tau_B)}{T_{(\theta_0, \tau_a = \tau_B)} T_{(\theta, \tau_a = \tau_B)} + S_{(\lambda, \tau_a = \tau_B)} [\rho^* - \rho_{Ray} - \rho_{Aer}(\tau_a = \tau_B)]} \\ &= \frac{T_{(\theta_0, \tau_a = \tau_B)} T_{(\theta, \tau_a = \tau_B)}}{[albedo_{min} / \cos(\theta_0) - \rho_{Ray} - \rho_{Aer}(\tau_a = \tau_B)] + S_{(\lambda, \tau_a = \tau_B)}} \end{aligned} \quad (16)$$

The background aerosol loading in the MAARM is based on

AERONET Level 2.0 AOT measurements made at the CAMS site in 2015. Time series plots of AOT at 440 and 675 nm are shown in Fig. 1. The MAARM uses the minimum AOT values as background aerosol loading values for the  $\rho_s$  retrieval. Fig. 1 shows that the background aerosol loading for the blue band is 0.028 and that for the red band is 0.020. In addition, time series plots of AOT from Xianghe are shown in Fig. S3, the yearly min AOT is 0.03 for red band and 0.028 for blue band. It can be found that the yearly min AOT from CAMS and Xianghe is very close. Thus, in this study we use the yearly min AOT 0.028 for red band and 0.02 for blue band as the background aerosol. Since the background aerosol loading is low, we use the single scattering approximation for  $\rho_{Aer}$  in Eqs. (15) and (16).

Applying Eq. (16) to Eq. (2), we change AOT ( $\tau_a$ ) by a given step size

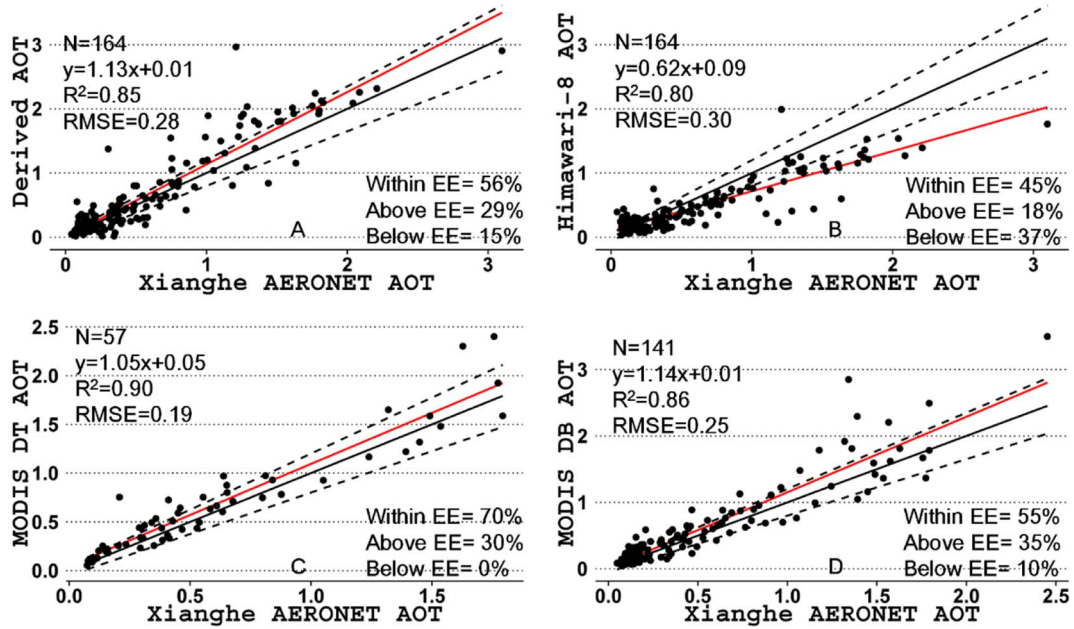


Fig. 8. Same as Fig. 6 but for the Xianghe site.

within a certain range to separately calculate the corresponding pseudo reflectance ( $\rho_{pseudo}$ ) for the blue and red bands. Thus:

$$\rho_{pseudo} = \left. \begin{aligned} & \frac{\omega_R \tau_R P_R(\mu, \mu_0, \phi - \phi_0)}{4\mu_0\mu} \\ & + \frac{\omega_0 \tau_a P_a(\mu, \mu_0, \phi - \phi_0)}{4\mu_0\mu} + R^{II} \\ & + \frac{T(\theta_0)T(\theta)\rho_s}{1 - \rho_s S(\lambda)} \end{aligned} \right\} \begin{aligned} & \rho_{Ray} \\ & \rho^a (Single + Multiple) \\ & \rho_s (albedo_{min}, \tau_B). \end{aligned} \quad (17)$$

The incremental interval for AOT is 0.01 with a range from 0 to 5.0, which is the same range used in the MODIS C6 DT land algorithm (Levy et al., 2007). In the MAARM, the 6 clustered categories are used as the candidate aerosol models in this method. Detailed parameters of the adopted models studied by Lee and Kim (2010) are shown in Table S1. The difference between  $\rho_{pseudo}$  and  $\rho^*$  is then calculated as:

$$\chi^2 = (\rho_{pseudo} - \rho^*)^2. \quad (18)$$

The AOT at blue and red bands are finally obtained as follows:

$$\left\{ \begin{aligned} \tau_a^{blue} &= \min(\chi_{blue}^2) & |\chi| < 0.25 \\ \tau_a^{red} &= \min(\chi_{red}^2) & |\chi| < 0.25 \\ \tau_a^{blue} &> \tau_a^{red} \end{aligned} \right. \quad (19)$$

According to Eq. (19), AOT can be estimated by minimizing  $\chi^2$ . If the minimum value of  $|\chi| > 0.25$ , the output of the MAARM AOT is set to null. This threshold value of  $|\chi|$  is the same one used in the DT algorithm where the QA flag is set to 0 when  $|\chi| > 0.25$ . The AE is then calculated using the Volz method (Soni et al., 2011) by blue and red band AOT. So that comparisons can be made with Himawari-8 Aerosol Property data, the AOT at these two bands are interpolated to 500 nm to obtain AOT at 500 nm. Finally, the FMF is calculated using the LUT-SDA with AOT at 500 nm and AE. It should be noted that Eqs. (17) and (18) are applied separately for all six candidate aerosol models listed in Table S1, and the aerosol models would be different for the two wavelengths by the result of Eq. (19).

Fig. 2 shows the flowchart describing the MAARM. The FMF is calculated using the LUT-SDA, which was developed for satellite images and uses AOT at two wavelengths to solve the FMF problem (Yan et al., 2017). This method is based on the SDA, which is currently used by AERONET for FMF calculations. The LUT-SDA builds an LUT to retrieve

the FMF using satellite-derived AOT and AE. Details about the algorithm are given in the Supplementary Fig. S3. To build an LUT, a set of hypothetical FMF and AE derivative values are imported to the SDA along with the satellite-determined AE to derive the AE of fine-mode aerosols. The LUT-SDA has been successfully applied to MODIS data not only on an urban scale (Beijing) but also for larger areas (Yan et al., 2017). The cloud detection scheme in the MAARM uses the Himawari-8 Cloud Property dataset and is based on the techniques developed by Ishida and Nakajima (2009), Ishida et al. (2011), Letu et al. (2014), and Nakajima et al. (2011).

### 3. Results and discussion

#### 3.1. Comparing MAARM- and 6S-derived aerosol reflectances

To test the performance of the aerosol reflectance approximation used in this study, results from Eq. (4) of the MAARM and from the 6S radiative transfer algorithm were compared. Aerosol reflectance in the 6S algorithm is calculated using the successive order of scattering method, which uses 12 G angles and 13 layers (Vermeete et al., 1997). Values for SSA and g at 550 nm (0.89 and 0.64, respectively) were taken from the continental aerosol model (Bevan et al., 2012). Fig. 3 shows MAARM- and 6S-derived aerosol reflectances as a function of AOT at 550 nm for four solar zenith angles (SZAs) (The satellite azimuth angle is 145°, satellite zenith angle is 53° and solar azimuth angle is 155°, which are corresponding to Himawari-8 geometry in Beijing-CAMS). Aerosol reflectances agree well when the SZA is equal to 30° and 45° (root-mean-square errors (RMSEs) of 0.012 and 0.007, respectively). The RMSE increases to 0.025 when the SZA is equal to 15° and 60°. This phenomenon also showed in the blue and red band (Figs. S5 and S6). These results also showed in Seidel et al. (2010), they found that HG approximation agrees well with 6S under the SZA from 20 to 45° but for 15° and 60° SZA the relative error is large in the two-order aerosol scattering approximation. This is because the different phase function used for this two method (the phase function of 6S is from Lorenz-Mie theory). Fig. 4A and B show MAARM-derived aerosol reflectance as a function of 6S-derived aerosol reflectance when AOT is equal to 0.5 and 1.5, respectively. Himawari-8 satellite geometry information was used in the calculations. Fig. 4C and D show the kernel density estimates corresponding to Fig. 4A and B. High kernel density values show

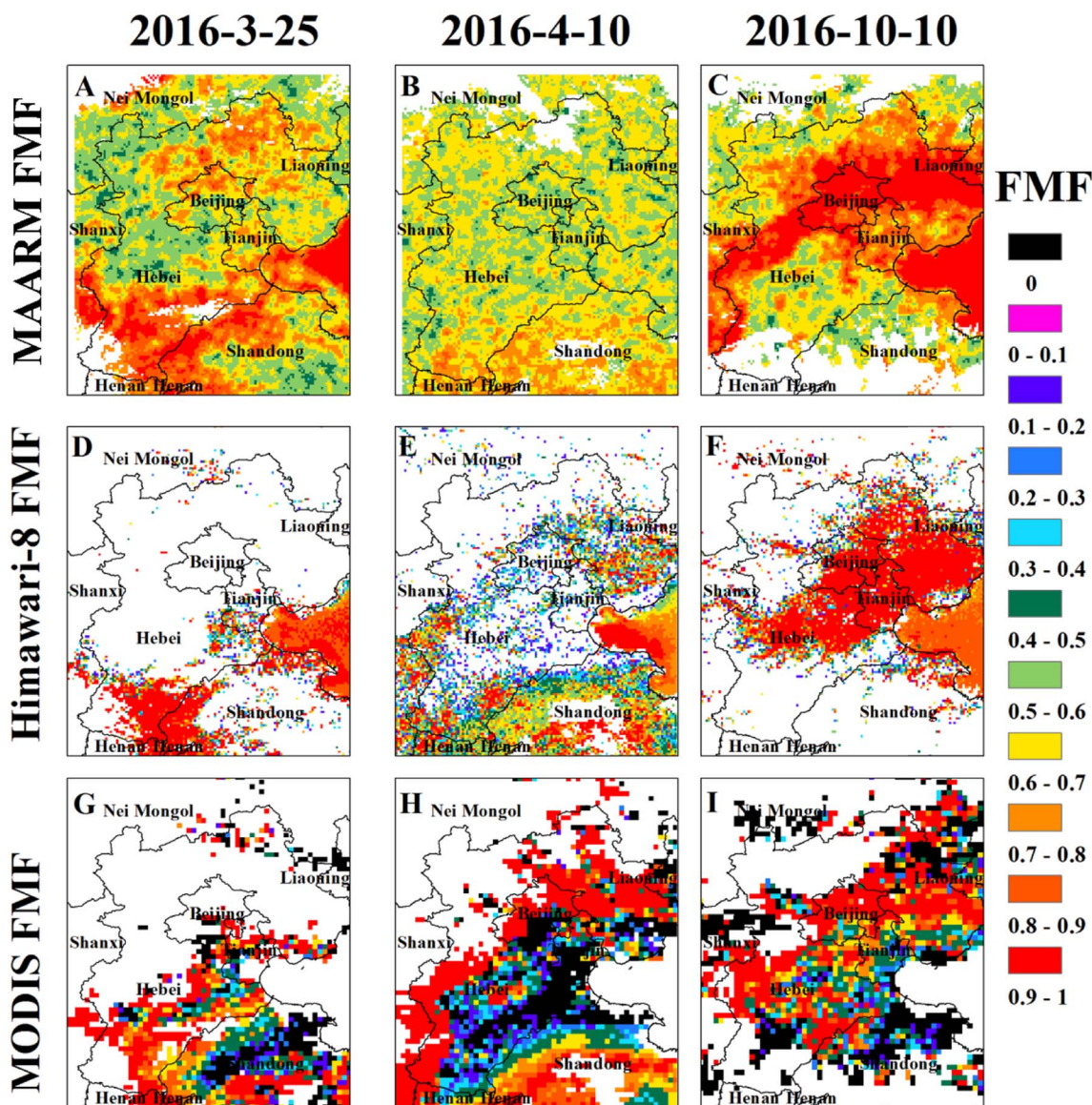


Fig. 9. Spatial distributions of the FMF retrieved from the MAARM (A–C), Himawari-8 (D–F), and the MODIS algorithm (G–I) on three days: 25 March 2016 (leftmost column), 10 April 2016 (middle column), and 10 October 2016 (rightmost column). All of the satellite images are acquired at 0310 coordinated universal time.

where most of the data lie. About 58% of the points seen in Fig. 4A ( $AOT = 0.5$ ) and 57% of the points seen in Fig. 4B ( $AOT = 1.5$ ) fall within the  $\pm 5\%$  estimated error (EE) envelope (based on Seidel et al. (2012)), we define the aerosol reflectance EE as  $\pm 5\%$  for this study). This suggests that there is a qualitative agreement between aerosol reflectances generated from the MAARM and the 6S algorithm.

In the MAARM, the contribution of molecular (Rayleigh) scattering is taken into account using single-scattering (Eq. (12)). However, multiple scattering by molecules is not negligible. Fig. S7 shows MAARM- and 6S-derived Rayleigh reflectances for 470 nm, 550 nm and 640 nm with solar zenith angles (SZAs) from 0 to 70°. It can be found that MAARM Rayleigh reflectances are lower than 6S's for these three wavelengths because it only uses the single-scattering approximation, especially at the short wavelength 470 nm. Thus, although the aerosol reflectance by MAARM can have a good accuracy compared with the 6S, its Rayleigh reflectances are underestimated.

### 3.2. AOT validation and comparison

Three retrieval results are presented in Fig. 5. On 25 March 2016, the AOT in the Beijing City area was  $< 0.2$  (Fig. 5A). Heavy aerosol

loading was found south of Hebei with AOT values  $> 1.0$ . To the east of Hebei, MAARM-estimated AOT ranged from 0.4–0.6. MODIS DB (Fig. 5G) and DT (Fig. 5J) retrievals have similar values, but lower values from Himawari-8 are seen (0.2–0.4; Fig. 5D). Although it was a cloud-free day, there are large gaps seen in MODIS DT AOT retrievals around Beijing (Fig. 5J). This may be because the surface reflectance was high due to a lack of green vegetation. Remer et al. (2005) have reported that the DT algorithm cannot successfully retrieve AOT over bright surfaces. On 10 April 2016 (Fig. 5B), MAARM-derived AOT was 0.4–0.6 in most areas around Beijing, Tianjin, and Hebei, similar to what is seen for MODIS DT retrievals (Fig. 5K). Himawari-8 AOT retrievals are smaller in magnitude (0.2–0.4). On 10 October 2016, the AOT was  $> 1.0$  in southern Beijing, Hebei, and Tianjin, which is consistent with the local haze conditions reported by weather stations on that day. Similar spatial characteristics on this day are also seen in MODIS DT AOT retrievals. Himawari-8 and MODIS DB AOT values were 0.4–0.8 in these regions. In general, the spatial coverage of MAARM performs better than the MODIS DT algorithm in urban areas where MAARM AOT retrievals can be made regardless of whether the pixel is bright or dark.

Although the input cloud mask is identical, there are some

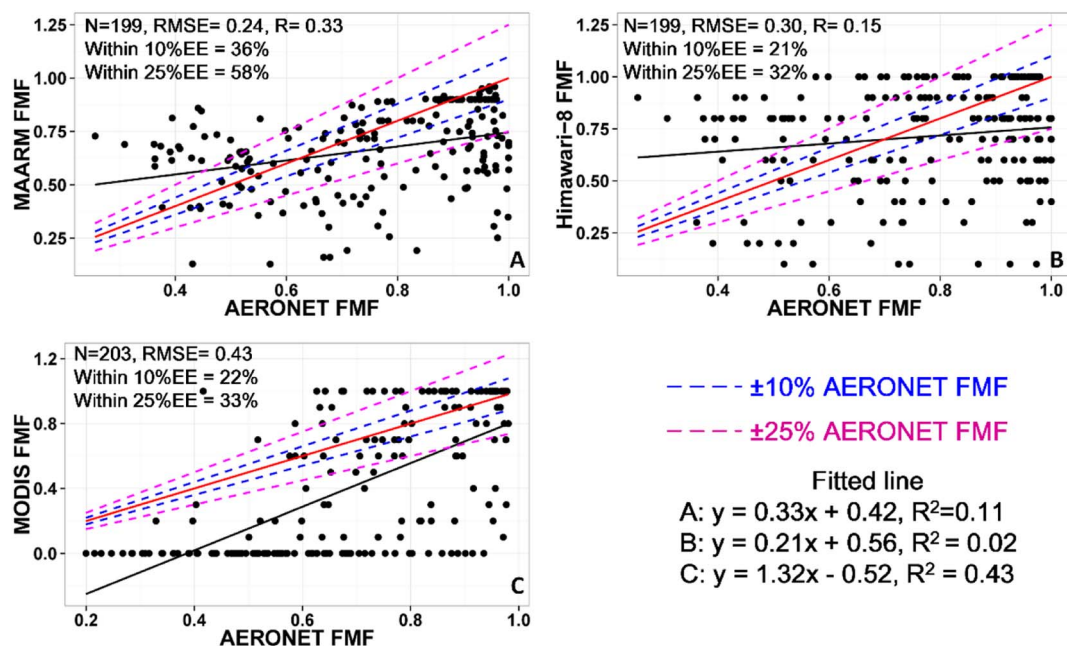


Fig. 10. (A) MAARM, (B) Himawari-8, and (C) MODIS FMF retrievals as a function of AERONET FMF. The solid red lines are the 1:1 lines and the solid black is the fitted line. The blue dashed lines are the estimated error (EE) envelope lines  $\pm 10\%$ AERONET FMF and the pink dashed lines are the EE envelope lines  $\pm 25\%$ AERONET FMF. The number of data points (N) and the root-mean-square errors (RMSE) are given. Based on Yan et al. (2017), we define the FMF EE as  $\pm 10\%$  and  $\pm 25\%$  for this study. (For interpretation of the references to color in this figure legend, the reader is referred to the web version of this article).

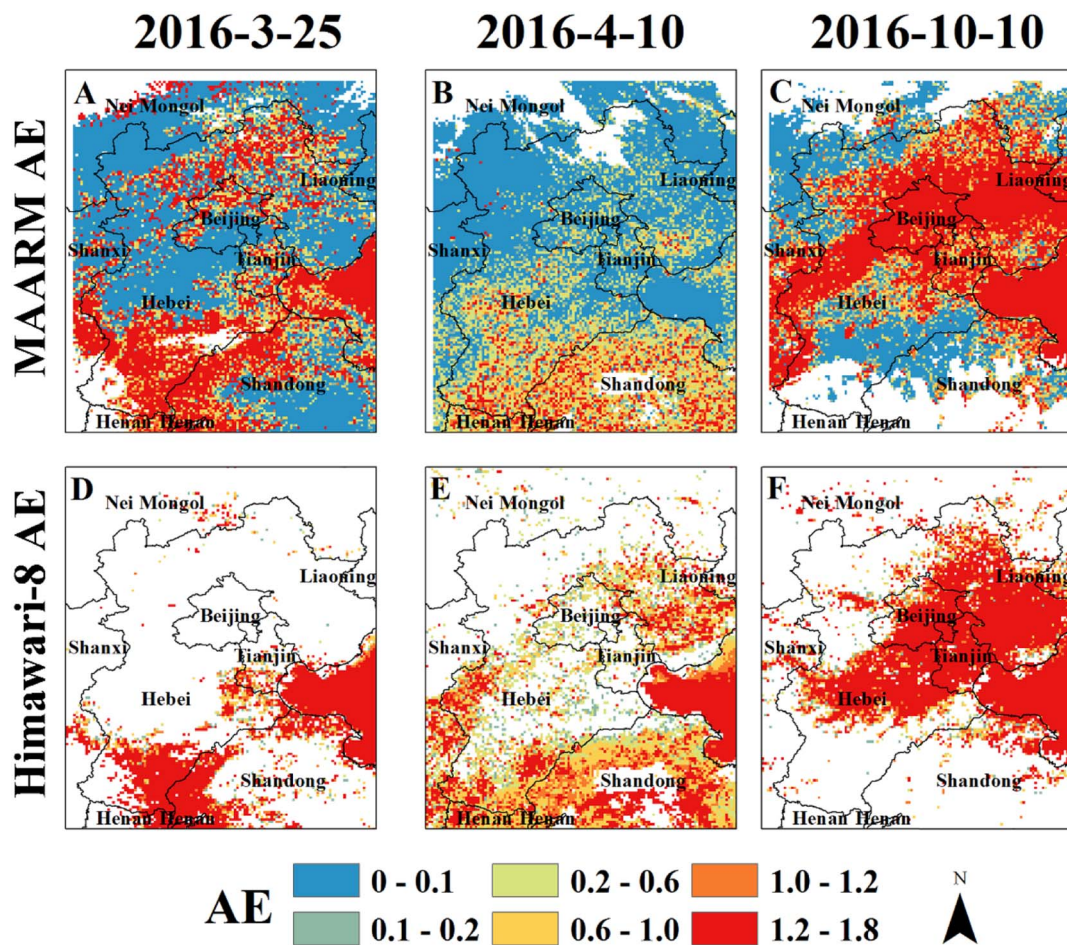


Fig. 11. Spatial distributions of the AE retrieved from (A–C) the MAARM and (D–F) Himawari-8 on three days: 25 March 2016 (leftmost column), 10 April 2016 (middle column), and 10 October 2016 (rightmost column).

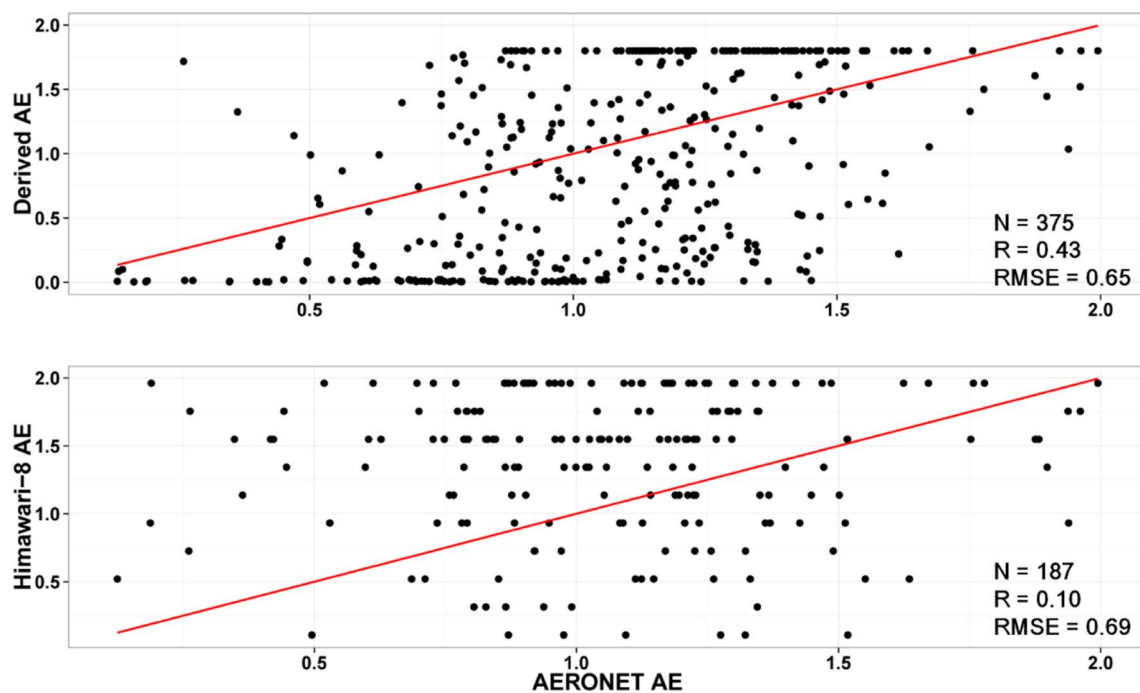


Fig. 12. MAARM (top) and Himawari-8 (bottom) AE retrievals as a function of AERONET AE. The solid red lines are the 1:1 lines. The number of data points (N), the correlation coefficients (R), and the root-mean-square errors (RMSE) are given. (For interpretation of the references to color in this figure legend, the reader is referred to the web version of this article).

differences in the spatial coverages of MAARM-retrieved AOT and Himawari-8 AOT. This is because only dark scenes (Band 6,  $R_{2,3} < 0.25$ ) are targeted for AOT retrievals over land in the Himawari-8 AOT retrieval algorithm (Daisaku, 2016). In addition, the surface reflectance in Band 3 ( $0.64\mu\text{m}$ ) is determined as a function of that in Band 6 ( $2.3\mu\text{m}$ ) in the Himawari-8 AOT retrieval algorithm. However, on days when there is heavy pollution, the use of near-infrared and red bands to derive the surface reflectance relationship is not appropriate (Wang et al., 2010; Yan et al., 2016). This will cause large uncertainties in the aerosol calculations and may make the final retrieval fail.

As shown in Fig. 5A and D, in northeastern Nei Mongol, the MAARM failed to retrieve AOT for some pixels. One reason is that the aerosol and Rayleigh reflectances ( $\rho_{Aer}$  and  $\rho_{Ray}$ ) were calculated using Eqs. (4) and (12), which may lead to  $\rho^* - \rho_{Aer} - \rho_{Ray} < 0$  for some pixels. Another reason may be that the output AOT did not meet the requirement that  $\tau_a^{blue} > \tau_a^{red}$  or  $|\chi| < 0.25$  in Eq. (19), which causes the retrieval to fail.

Figs. 6–8 show the MAARM AOT, Himawari-8 AOT, MODIS DT AOT, and MODIS DB AOT as a function of AERONET AOT for Beijing, CAMS, and Xianghe. Level 2 AERONET data were collected over the course of  $\pm 2$  to 30 min around the satellite observation times. The dotted red line is the EE envelope line  $\pm (0.05 + 0.15 \times \text{AERONET AOT})$  and the solid red line is the 1:1 line. Figs. 6A and 7A show that 57% (number of samples,  $N = 139$ ,  $\text{RMSE} = 0.18$ ) and 57% ( $N = 165$ ,  $\text{RMSE} = 0.23$ ) of the MAARM retrievals are within the EE envelope at the Beijing and CAMS sites. Thirty-two percent (Beijing,  $N = 139$ ,  $\text{RMSE} = 0.27$ ) and 34% (CAMS,  $N = 165$ ,  $\text{RMSE} = 0.31$ ) of Himawari-8 AOT retrievals fall within the EE envelope (Figs. 6B and 7B). The Beijing and CAMS AERONET stations are located in urban areas where the surface is complex and mixed. Much uncertainty would be generated by these surfaces, which makes it difficult for satellites to provide accurate AOT retrievals over these areas. This is also seen in MODIS DT AOT retrievals where 33% (Beijing,  $N = 60$ ,  $\text{RMSE} = 0.18$ ) and 37% (CAMS,  $N = 46$ ,  $\text{RMSE} = 0.43$ ) of retrievals fall within the EE envelope (Figs. 6C and 7C). Nichol and Bilal (2016) found that only 20.42% of the MODIS DT AOTs from 2002 to 2014 at the Beijing AERONET site were within the EE envelope. MODIS DB AOT retrievals performed

better in these urban areas with 66% (Beijing,  $N = 109$ ,  $\text{RMSE} = 0.10$ ) and 63% (CAMS,  $N = 95$ ,  $\text{RMSE} = 0.12$ ) of retrievals falling within the EE envelope (Figs. 6D and 7D). At Xianghe, which is located in a rural area, MAARM AOT retrievals were also more accurate than the Himawari-8 AOT retrievals with 56% of MAARM retrievals and 45% of Himawari-8 retrievals falling within the EE envelope (Fig. 8A and B). There was a considerable improvement for MODIS DT AOT retrievals with 70% of retrievals falling within the EE envelope ( $N = 57$ ,  $\text{RMSE} = 0.19$ ). As for MODIS DB AOT retrievals, 55% ( $N = 141$ ,  $\text{RMSE} = 0.25$ ) of them fall within the EE envelope.

### 3.3. FMF validation and comparison

Fig. 9 shows the MAARM-derived FMF for the same dates shown in Fig. 5. On 25 March 2016, high values of FMF (0.9–1) were found south of Hebei (Fig. 9A, D, and G). Himawari-8 FMF retrievals were mostly missing in and around Beijing and north of Hebei. On 10 April 2016, the MAARM- and MODIS-derived FMF in Shandong was high (0.9–1.0). However, the spatial coverage of the Himawari-8 FMF retrievals on this day was poor. On 10 October 2016, MAARM and Himawari-8 FMF retrievals were similar in Beijing, Tianjin and east of Hebei (0.9–1). However, in the center of Hebei, the MAARM-derived FMF ranged from 0.5–0.7 while the Himawari-8 FMF retrievals ranged from 0.9–1.0. MAARM and MODIS retrievals showed high FMF values in Beijing and west of Hebei (Fig. 9C and I). Zero values were seen in many MODIS pixels (Fig. 9I). Yan et al. (2017) found that this issue limited the application of MODIS FMF retrievals because a pure coarse-mode AOT (FMF = 0) in an urban area is rare.

A comparison of Figs. 5 and 9 shows that there are Himawari-8 AOT retrievals in places where no FMFs are retrieved. This is because only pixels with  $\text{AE} > 0$  have FMF values in the Himawari-8 aerosol product. As shown in Fig. 11D, E, and F, the spatial coverages of FMF and AE are identical.

Fig. 10 shows the validation results for the MAARM, Himawari-8, and MODIS FMF retrievals using AERONET data as the ground truth. Thirty-six percent of MAARM FMF retrievals fall within the  $\pm 10\%$  AERONET FMF envelope while 21% of the Himawari-8 FMF retrievals

and 22% of the MODIS FMF retrievals fall within the  $\pm 10\%$  AERONET FMF envelope. The RMSE for the MAARM FMF retrievals is 0.24, which is less than that for the Himawari-8 and MODIS FMF retrievals (0.30 and 0.43, respectively). When the EE envelope was extended to  $\pm 25\%$  AERONET FMF, the MAARM FMF retrievals also showed a better performance than the Himawari-8 and MODIS FMF retrievals with 58% of the retrievals falling within the  $\pm 25\%$  AERONET FMF envelope, compared with 32% for the Himawari-8 FMF retrievals and 33% for the MODIS FMF retrievals. Although some improvements achieved by MAARM FMF compared with Himawari-8 FMF and MODIS FMF, it is still lack of skill in determining FMF and the retrieval results are not recommended to use at this time.

### 3.4. AE validation and comparison

The AE has been used in various studies as a tool to estimate the particle size distribution as well as to distinguish between different types of aerosols (Jung and Kim, 2013; Lodhi et al., 2013; O'Neill et al., 2001a). It is also an indicator of the average aerosol particle size in the atmosphere (Soni et al., 2011). In general, an  $AE \leq 1$  indicates an aerosol size distribution mainly dominated by coarse-mode aerosols, while an  $AE \geq 1$  usually indicates a size distribution dominated by fine-mode aerosols (Eck et al., 1999). The MAARM-derived AE is shown in Fig. 11A–C. To avoid the retrieval of unphysical values, the MAARM assigns a maximum AE value of 1.8. This fix is the same as that used in the DB method (Sayer et al., 2013). As shown in Fig. 11C, 10 October 2016 was a hazy day with high values of AE (1.2–1.8) observed in Beijing, Tianjin, and east of Hebei. Eck et al. (1999) deemed that  $AE \geq 1$  is usually associated with urban pollution and biomass burning. High AE values in Beijing and Tianjin are due to the rapid development of urbanized construction in this region, which has led to severe  $PM_{2.5}$  pollution (Quan et al., 2011; Tao et al., 2012). Fig. 11A and B show that high AE values are also seen in Shandong Province. In Shandong Province, heavy crop-burning emissions have been reported due to the open burning of wheat straw and maize in rural areas (Ni et al., 2015). MAARM AE retrievals are comparable to Himawari-8 AE retrievals (Fig. 11D–F). Himawari-8 AE values less than or equal to zero are not shown. There is a good agreement between the spatial distributions of MAARM and Himawari-8 AE retrievals. However, there are numerous missing Himawari-8 AE values, which cover most of Beijing and Hebei.

Fig. 12 shows the validation results for the MAARM and Himawari-8 AE retrievals using AERONET data as the ground truth. To avoid uncertainties in AE that arise when the AOTs are small, only AE retrievals associated with  $AOT > 0.15$  are shown (Gobbi et al., 2007). In contrast to the AOT validation, MAARM and Himawari-8 AE retrievals are more scattered. The correlation coefficient for the relationship between MAARM and AERONET AE retrievals is 0.43 and the RMSE is 0.65 ( $N = 375$ ). Little correlation is seen between Himawari-8 and AERONET AE retrievals ( $R = 0.1$ ). The RMSE is 0.69 ( $N = 187$ ).

### 3.5. Discussion

In general, surface reflectance is an important aspect of AOT retrievals. Surface reflectance is used to differentiate between signals from aerosols and the land surface. Kaufman et al. (1997) reported that an error of 0.01 in surface reflectance can lead to an error of 0.1 in retrieved AOT values. In this study, the surface reflectance was calculated using the minimum albedo over 30 days and the radiative transfer equation. This procedure is similar to the minimum reflectance technique, which is considered to be a reliable and accurate method to retrieve AOT and has been applied to satellite data (Herman and Celarier, 1997; Knapp, 2002; Knapp et al., 2002; Koelemeijer et al., 2003; Wong et al., 2011). However, the minimum reflectance method has its limitations. Knapp et al. (2005) showed that cloud shadows and terrain can lead to incorrect values of the minimum reflectance and can ultimately impact the retrieved AOT accuracy. Another issue for AOT

retrievals is the radiative transfer equation. A modified radiative transfer equation in the MAARM that considers multiple aerosol scattering impacts and minimizes the complexity was developed in this study. The modified radiative transfer equation for aerosol reflectance is fast and simple compared with the 6S radiative transfer algorithm (Figs. 3 and 4) and is accurate with low RMSEs under real satellite geometry conditions (overall error within 5%). However, the contribution of molecular (Rayleigh) scattering is taken into account using only single-scattering in MAARM. As shown in Fig. S7, the Rayleigh reflectance of MAARM is underestimated compared with 6S's, especially at the short wavelength of 470 nm.

Since it is not always possible to constrain aerosol model information from satellites themselves (Kokhanovsky et al., 2007), this study used an empirical Asian aerosol model (Lee and Kim, 2010) for AOT retrievals. However, Bi et al. (2016) showed that significant differences could arise on high aerosol loading days when using this aerosol model. For example,  $g$  values under dust conditions can be significantly higher ( $0.742 \pm 0.008$  under pure dust conditions and  $0.723 \pm 0.009$  under transported anthropogenic dust conditions). So the empirical aerosol model can be a source of error in MAARM retrievals of AOT.

The validation of FMF retrievals shown in Fig. 10 shows that the MAARM performed better than the Himawari-8 algorithm (with 36% of the data falling within  $\pm 10\%$  AERONET FMF and 58% of the data falling within  $\pm 25\%$  AERONET FMF as opposed to 21% of the Himawari-8 data falling within  $\pm 10\%$  AERONET FMF and 32% of the Himawari-8 data falling within  $\pm 25\%$  AERONET FMF). Comparing Fig. 5D–F with Fig. 9D–F, Himawari-8 generally failed to retrieve the FMF even though the AOT was successfully retrieved. Full coverage of both AOT and the FMF was possible using the MAARM when AOT information was available. In contrast to the AOT retrieval, high accuracy in FMF retrievals is still difficult to obtain from satellite images, as discussed by Yan et al. (2017). This is because satellite-based AE retrievals, which provide size information about aerosols, have many uncertainties (Alvim et al., 2017). As shown in Fig. 12, the correlation between the MAARM- and AERONET-retrieved AE was not high ( $R = 0.49$ ). Hasekamp and Landgraf (2007) showed that single-viewing-angle measurements of intensity alone did not provide sufficient information about aerosol properties. This limitation also affects other aerosol products. Sayer et al. (2013) reported that the latest MODIS C6 DB AOT had a strong correlation with the AERONET AOT ( $R = 0.93$ ) while the AE's correlation was much weaker ( $R = 0.45$ ). Levy et al. (2013) also found little quantitative skill in MODIS-retrieved aerosol size parameters over land. As a result, in the C6 aerosol product, the AE over land (based on the DT algorithm) was removed. Therefore, a reliable method for retrieving AE needs to be developed for single-viewing-angle measurements, such as those made by Himawari-8 and MODIS.

## 4. Conclusions

This study presents a satellite-based algorithm (MAARM) for retrieving aerosol properties with particular attention given to Himawari-8 satellite images. This method based on a modified radiative transfer equation and the minimum albedo can directly output AOT, FMF, and AE information. The developed modified radiative transfer equation in MAARM is simple and had been validated with the 6S radiative transfer algorithm. The percent error achieved by this modified radiative transfer equation for aerosol reflectance calculations is  $\sim 5\%$  under real Himawari-8 geometry conditions, which suggests a good accuracy. However, although the aerosol reflectance by MAARM can have a good accuracy compared with the 6S, its Rayleigh reflectances are underestimated because it only use single-scattering approximation.

The results of the validation showed that an improvement was achieved by the MAARM in retrieving AOT, FMF and AE compared with Himawari-8 retrievals. The MAARM-derived AOT had a higher level of accuracy (Beijing: 57%, CAMS: 57%, and Xianghe: 56% within the EE

envelope) than the Himawari-8 AOT (Beijing: 32%, CAMS: 34%, and Xianghe: 45% within the EE envelope). By incorporating the LUT-SDA, the MAARM also had better outcomes for FMF (36% within  $\pm 10\%$ AERONET FMF and 58% within  $\pm 25\%$ AERONET FMF), compared with Himawari-8 FMF retrievals (21% within  $\pm 10\%$ AERONET FMF and 32% within  $\pm 25\%$ AERONET FMF). Although the MAARM produced reasonable AOT retrievals, the AE was generally less precise ( $R = 0.43$  and  $RMSE = 0.65$ ). Uncertainties in the Himawari-8 AE retrievals were also found. The correlation coefficient of the relationship between Himawari-8 and AERONET AE retrievals was 0.1 and the RMSE was 0.69.

This study demonstrates that an overall improvement was achieved by the MAARM in retrieving AOT, FMF, and AE compared with Himawari-8 standard aerosol property retrievals. However, the MAARM still remains a distinct lack of skill in determining FMF and AE. Thus, FMF and AE use from the MAARM retrieval is not recommended at this time. Owing to the high temporal resolution of Himawari-8, the MAARM can detect more frequently variations in aerosol properties not only at urban scales, but also over larger areas.

## Acknowledgements

This work was supported by the National Key Research and Development Plan of China (2017YFC1501702), the National Science Foundation of China (41675141, 41375155) and the National Basic Research Program (973 Program) of China (2013CB955804). The authors gratefully acknowledge the MODIS and AERONET teams for their effort in making the data available. We would like to thank the Meteorological Satellite Center (MSC) of the Japan Meteorological Agency (JMA) for providing Himawari-8 data. The authors thank the reviewers for their constructive detailed comments and suggestions related to this paper.

## Appendix A. Supplementary data

Supplementary data to this article can be found online at <https://doi.org/10.1016/j.atmosres.2018.02.021>.

## References

- Ahn, C., Torres, O., Bhartia, P.K., 2008. Comparison of ozone monitoring instrument UV aerosol products with aqua/moderate resolution imaging spectroradiometer and multiangle imaging spectroradiometer observations in 2006. *J. Geophys. Res.-Atmos.* 113 (D16). <http://dx.doi.org/10.1029/2007JD008832>.
- Alvim, D.S., Pendharkar, J., Capistrano, V.B., Frassoni, A., Enoré, D.P., Neto, O.L.D.M., et al., 2017. Aerosol distribution over Brazil with ECHAM-HAM and CAM5-MAM3 simulations and its comparison with ground-based and satellite data. *Atmos. Pollut. Res.* 8 (4), 718–728.
- Antoine, D., Morel, A., 1998. Relative importance of multiple scattering by air molecules and aerosols in forming the atmospheric path radiance in the visible and near infrared parts of the spectrum. *Appl. Opt.* 37 (12), 2245–2259. <http://dx.doi.org/10.1364/AO.37.002245>.
- Bell, M.L., Ebisu, K., Belanger, K., 2007. Ambient air pollution and low birth weight in Connecticut and Massachusetts. *Environ. Health Perspect.* 115, 1118–1124. <http://dx.doi.org/10.1289/ehp.9759>.
- Bellouin, N., Boucher, O., Haywood, J., Reddy, M.S., 2005. Global estimates of aerosol direct radiative forcing from satellite measurements. *Nature* 438, 1138–1141. <http://dx.doi.org/10.1038/nature04348>.
- Bessho, K., Date, K., Hayashi, M., Ikeda, A., Imai, T., Inoue, H., ... Yoshida, R., 2016. An introduction to Himawari-8/9 - Japan's new-generation geostationary meteorological satellites. *J. Meteorol. Soc. Japan Ser. II* 94 (2), 151–183. <http://dx.doi.org/10.2151/jmsj.2016-009>.
- Bevan, S.L., North, P.R., Los, S.O., Grey, W.M., 2012. A global dataset of atmospheric aerosol optical depth and surface reflectance from AATSR. *Remote Sens. Environ.* 116, 199–210. <http://dx.doi.org/10.1016/j.rse.2011.05.024>.
- Bi, J., Huang, J., Holben, B., Zhang, G., 2016. Comparison of key absorption and optical properties between pure and transported anthropogenic dust over East and Central Asia. *Atmos. Chem. Phys.* 16 (24), 15501–15516. <http://dx.doi.org/10.5194/acp-16-15501-2016>.
- Bilal, M., Nichol, J.E., Bleiweiss, M.P., Dubois, D., 2013. A simplified high resolution MODIS Aerosol Retrieval Algorithm (SARA) for use over mixed surfaces. *Remote Sens. Environ.* 136, 135–145. <http://dx.doi.org/10.1016/j.rse.2013.04.014>.
- Daisaku, U., 2016. Aerosol optical depth product derived from Himawari-8 data for Asian dust monitoring. *Meteorol. Satell. Cent. Tech. Note* 61, 59–63.
- Drury, E., Jacob, D.J., Wang, J., Spurr, R.J.D., Chance, K., 2008. Improved algorithm for modis satellite retrievals of aerosol optical depths over western North America. *J. Geophys. Res.-Atmos.* 113 (D16), 280–288. <http://dx.doi.org/10.1029/2007JD009573>.
- Eck, T.F., Holben, B.N., Reid, J.S., Dubovik, O., Smirnov, A., O'Neill, N.T., ... Kinne, S., 1999. Wavelength dependence of the optical depth of biomass burning, urban, and desert dust aerosols. *J. Geophys. Res.-Atmos.* 104 (D24) (333–331). <https://doi.org/10.1029/1999JD900923>.
- Fukuda, S., Nakajima, T., Takenaka, H., Higurashi, A., Kikuchi, N., Nakajima, T.Y., Ishida, H., 2013. New approaches to removing cloud shadows and evaluating the 380 nm surface reflectance for improved aerosol optical thickness retrievals from the GOSAT/TANSO-Cloud and Aerosol imager. *J. Geophys. Res.-Atmos.* 118 (24), 13,520–13,531. <http://dx.doi.org/10.1002/2013JD020090>.
- Gobbi, G.P., Kaufman, Y.J., Koren, I., Eck, T.F., 2007. Classification of aerosol properties derived from AERONET direct sun data. *Atmos. Chem. Phys. Discuss.* 7 (2), 8713–8726.
- Hansen, J.E., Travis, L.D., 1974. Light scattering in planetary atmospheres. *Space Sci. Rev.* 16 (4), 527–610. <http://dx.doi.org/10.1007/BF00168069>.
- Hasekamp, O.P., Landgraf, J., 2007. Retrieval of aerosol properties over land surfaces: capabilities of multiple-viewing-angle intensity and polarization measurements. *Appl. Opt.* 46, 3332–3344. <http://dx.doi.org/10.1364/AO.46.003332>.
- Herman, J.R., Celarier, E.A., 1997. Earth surface reflectivity climatology at 340–380 nm from TOMS data. *J. Geophys. Res.-Atmos.* 102 (D23), 28,003–28,011. <http://dx.doi.org/10.1029/97JD02074>.
- Higurashi, A., Nakajima, T., 1999. Development of a two-channel aerosol retrieval algorithm on a global scale using NOAA/AVHRR. *J. Atmos. Sci.* 56 (56), 924–941. [http://dx.doi.org/10.1175/1520-0469\(1999\)056<0924:DOATCA>2.0.CO;2](http://dx.doi.org/10.1175/1520-0469(1999)056<0924:DOATCA>2.0.CO;2).
- Higurashi, A., Nakajima, T., 2002. Detection of aerosol types over the East China Sea near Japan from four-channel satellite data. *Geophys. Res. Lett.* 29 (17) (17-1–17-4). <https://doi.org/10.1029/2002GL015357>.
- Holben, B.N., Eck, T.F., Slutsker, I., Tanré, D., Buis, J.P., Setzer, A., ... Smirnov, A., 1998. AERONET—a federated instrument network and data archive for aerosol characterization. *Remote Sens. Environ.* 66 (1), 1–16. [http://dx.doi.org/10.1016/S0034-4257\(98\)00031-5](http://dx.doi.org/10.1016/S0034-4257(98)00031-5).
- Holben, B.N., Tanré, D., Smirnov, A., Eck, T.F., Slutsker, I., Abuhassan, N., ... Zibordi, G., 2001. An emerging ground-based aerosol climatology: aerosol optical depth from AERONET. *J. Geophys. Res.-Atmos.* 106 (D11), 12,067–12,097. <http://dx.doi.org/10.1029/2001JD900014>.
- Hsu, N.C., Jeong, M.J., Bettenhausen, C., Sayer, A.M., Hansell, R., Seftor, C.S., ... Tsay, S.-C., 2013. Enhanced deep blue aerosol retrieval algorithm: the second generation. *J. Geophys. Res.-Atmos.* 118 (16), 9296–9315. <http://dx.doi.org/10.1002/jgrd.50712>.
- Huang, J., Kondragunta, S., Laszlo, I., Liu, H., Remer, L.A., Zhang, H., ... Petrenko, M., 2016. Validation and expected error estimation of Suomi-NPP VIIRS aerosol optical thickness and Ångström exponent with AERONET. *J. Geophys. Res.-Atmos.* 121 (12), 7139–7160. <http://dx.doi.org/10.1002/2016JD024834>.
- Ishida, H., Nakajima, T.Y., 2009. Development of an unbiased cloud detection algorithm for a spaceborne multispectral imager. *J. Geophys. Res.-Atmos.* 114 (D7), 1291–1298. <http://dx.doi.org/10.1029/2008JD010710>.
- Ishida, H., Nakajima, T.Y., Yokota, T., Kikuchi, N., Watanabe, H., 2011. Investigation of GOSAT TANSO-CAI cloud screening ability through an intersatellite comparison. *J. Appl. Meteorol. Climatol.* 50 (7), 1571–1586. <http://dx.doi.org/10.1175/2011JAMC2672.1>.
- Jethva, H., Torres, O., Ahn, C., 2014. Global assessment of OMI aerosol single-scattering albedo using ground-based AERONET inversion. *J. Geophys. Res.-Atmos.* 119, 9020–9040. <http://dx.doi.org/10.1002/2014JD021672>.
- Jung, C.H., Kim, Y.P., 2013. Analytic solution on the estimation of the Ångström exponent in log-normal aerosol size distribution. *Part. Sci. Technol.* 31 (1), 92–99. <http://dx.doi.org/10.1080/02726351.2012.658902>.
- Kahn, R.A., Gaitley, B.J., Garay, M.J., Diner, D.J., Eck, T.F., Smirnov, A., Holben, B.N., 2010. Multiangle imaging spectroradiometer global aerosol product assessment by comparison with the Aerosol Robotic Network. *J. Geophys. Res.-Atmos.* 115 (D23). <http://dx.doi.org/10.1029/2010JD014601>.
- Kaufman, Y.J., Tanré, D., Gordon, H.R., Nakajima, T., Lenoble, J., Frouin, R., ... Teillet, P.M., 1997. Passive remote sensing of tropospheric aerosol and atmospheric correction for the aerosol effect. *J. Geophys. Res.-Atmos.* 102 (D14), 16,815–16,830. <http://dx.doi.org/10.1029/97JD01496>.
- Knapp, K.R., 2002. Quantification of aerosol signal in GOES 8 visible imagery over the United States. *J. Geophys. Res.-Atmos.* 107 (D20) (AAC 4-1–AAC 4-11). <https://doi.org/10.1029/2001JD002001>.
- Knapp, K.R., Vonder Haar, T.H., Kaufman, Y.J., 2002. Aerosol optical depth retrieval from GOES-8: uncertainty study and retrieval validation over South America. *J. Geophys. Res.-Atmos.* 107 (D7) (AAC 2-1–AAC 2-12). <https://doi.org/10.1029/2001JD000505>.
- Knapp, K.R., Frouin, R., Kondragunta, S., Prados, A., 2005. Toward aerosol optical depth retrievals over land from GOES visible radiances: determining surface reflectance. *Int. J. Remote Sens.* 26, 4097–4116. <http://dx.doi.org/10.1080/01431160500099329>.
- Koelemeijer, R.B.A., De Haan, J.F., Stammes, P., 2003. A database of spectral surface reflectivity in the range 335–772 nm derived from 5.5 years of GOME observations. *J. Geophys. Res.-Atmos.* 108 (D2) (ACH 8-1–ACH 8-13). <https://doi.org/10.1029/2002JD002429>.
- Kokhanovsky, A.A., Breon, F.M., Cacciari, A., 2007. Aerosol remote sensing over land: a comparison of satellite retrievals using different algorithms and instruments. *Atmos. Res.* 85 (3), 372–394. <http://dx.doi.org/10.1016/j.atmosres.2007.02.008>.
- Lee, K.H., Kim, Y.J., 2010. Satellite remote sensing of Asian aerosols: a case study of

- clean, polluted and dust storm days. *Atmos. Meas. Tech. Discuss.* 3 (6), 1771–1784. <http://dx.doi.org/10.5194/amt-3-1771-2010>.
- Letu, H., Nagao, T.M., Nakajima, T.Y., Matsumae, Y., 2014. Method for validating cloud mask obtained from satellite measurements using ground-based sky camera. *Appl. Opt.* 53 (31), 7523–7533. <http://dx.doi.org/10.1364/AO.53.007523>.
- Levy, R.C., Remer, L.A., Mattoo, S., Vermote, E.F., Kaufman, Y.J., 2007. Second-generation operational algorithm: retrieval of aerosol properties over land from inversion of moderate resolution imaging spectroradiometer spectral reflectance. *J. Geophys. Res.-Atmos.* 112 (D13), 319–321. <http://dx.doi.org/10.1029/2006JD007811>.
- Levy, R.C., Remer, L.A., Tanré, D., Mattoo, S., Kaufman, Y.J., 2009. Algorithm for Remote Sensing of Tropospheric Aerosol Over Dark Targets From MODIS: Collections 005 and 051: Revision 2; Feb 2009, MODIS Algorithm Theoretical Basis Document.
- Levy, R.C., Remer, L.A., Kleidman, R.G., Mattoo, S., Ichoku, C., Kahn, R., Eck, T.F., 2010. Global evaluation of the Collection 5 MODIS dark-target aerosol products over land. *Atmos. Chem. Phys.* 10, 10,399–10,420. <http://dx.doi.org/10.5194/acp-10-10399-2010>.
- Levy, R.C., Mattoo, S., Munchak, L.A., Remer, L.A., Sayer, A.M., Patadia, F., Hsu, N.C., 2013. The Collection 6 MODIS aerosol products over land and ocean. *Atmos. Meas. Tech.* 6, 2989–3034. <http://dx.doi.org/10.5194/amt-6-2989-2013>.
- Li, S., Chen, L., Xiong, X., Tao, J., Su, L., Han, D., Liu, Y., 2013. Retrieval of the haze optical thickness in North China Plain using MODIS data. *IEEE Trans. Geosci. Remote Sens.* 51 (5), 2528–2540. <http://dx.doi.org/10.1109/TGRS.2012.2214038>.
- Liu, C.H., Liu, G.R., 2009. Aerosol optical depth retrieval for SPOT HRV images. *J. Mar. Sci. Technol.* 17, 300–305.
- Liu, B., Ma, Y., Gong, W., Zhang, M., Yang, J., 2018. Study of continuous air pollution in winter over Wuhan based on ground-based and satellite observations. *Atmos. Pollut. Res.* 9, 156–165.
- Lodhi, N.K., Beegum, S.N., Singh, S., Kumar, K., 2013. Aerosol climatology at Delhi in the western Indo-Gangetic Plain: microphysics, long-term trends, and source strengths. *J. Geophys. Res.-Atmos.* 118 (3), 1361–1375. <http://dx.doi.org/10.1002/jgrd.50165>.
- Luo, N., An, L., Nara, A., Yan, X., Zhao, W., 2016. GIS-based multi-element source analysis of dustfall in Beijing: a study of 40 major and trace elements. *Chemosphere* 152, 123–131. <http://dx.doi.org/10.1016/j.chemosphere.2016.02.099>.
- Munchak, L.A., Levy, R.C., Mattoo, S., Remer, L.A., 2013. MODIS 3 km aerosol product: applications over land in an urban/suburban region. *Atmos. Meas. Tech.* 6 (7), 1747–1759. <http://dx.doi.org/10.5194/amt-6-1747-2013>.
- Murakami, H., 2016. Ocean color estimation by Himawari-8/AHI. In: Frouin, R.J., Shenoi, S.C., Rao, K.H. (Eds.), *Remote Sensing of the Oceans and Inland Waters: Techniques, Applications, and Challenges*. Vol. 9878 SPIE, Bellingham, WA and Cardiff, Wales. <http://dx.doi.org/10.1117/12.2225422>.
- Nakajima, T.Y., Tsuchiya, T., Ishida, H., Matsui, T.N., Shimoda, H., 2011. Cloud detection performance of spaceborne visible-to-infrared multispectral imagers. *Appl. Opt.* 50 (17), 2601–2616. <http://dx.doi.org/10.1364/AO.50.002601>.
- Ni, H.Y., Han, Y.M., Cao, J.J., Chen, L.W.A., Tian, J., Wang, X.L., ... Huang, R.J., 2015. Emission characteristics of carbonaceous particles and trace gases from open burning of crop residues in China. *Atmos. Environ.* 123, 399–406. <http://dx.doi.org/10.1016/j.atmosenv.2015.05.007>.
- Nichol, J., Bilal, M., 2016. Validation of MODIS 3 km resolution aerosol optical depth retrievals over Asia. *Remote Sens.* 8, 328–336. <http://dx.doi.org/10.3390/rs8040328>.
- O'Neill, N.T., Eck, T.F., Holben, B.N., Smirnov, A., Dubovik, O., Royer, A., 2001a. Bimodal size distribution influences on the variation of Ångström derivatives in spectral and optical depth space. *J. Geophys. Res.-Atmos.* 106, 9787–9806. <http://dx.doi.org/10.1029/2000JD900245>.
- O'Neill, N.T., Dubovik, O., Eck, T.F., 2001b. Modified Ångström exponent for the characterization of submicrometer aerosols. *Appl. Opt.* 40, 2368–2375. <http://dx.doi.org/10.1364/AO.40.002368>.
- O'Neill, N.T., Eck, T.F., Smirnov, A., Holben, B.N., Thulasiraman, S., 2003. Spectral discrimination of coarse and fine mode optical depth. *J. Geophys. Res.-Atmos.* 108 (D17). <http://dx.doi.org/10.1029/2002JD002975>.
- Patadia, F., Kahn, R.A., Limbacher, J.A., Burton, S.P., Ferrare, R.A., Hostetler, C.A., Hair, J.W., 2013. Aerosol airmass type mapping over the urban Mexico City region from space-based multi-angle imaging. *Atmos. Chem. Phys.* 13 (18), 9525–9541. <http://dx.doi.org/10.5194/acp-13-9525-2013>.
- Penner, J.E., Dickinson, E.R., O'Neill, A.C., 1992. Effects of aerosol from biomass burning on the global radiation budget. *Science* 256, 1432–1434. <http://dx.doi.org/10.1126/science.256.5062.1432>.
- Pope III, C.A., Burnett, R.T., Thun, M.J., Calle, E.E., Krewski, D., Ito, K., Thurston, G.D., 2002. Lung cancer, cardiopulmonary mortality, and long-term exposure to fine particulate air pollution. *J. Am. Med. Assoc.* 287, 1132–1141. <http://dx.doi.org/10.1001/jama.287.9.1132>.
- Quan, J., Zhang, Q., He, H., Liu, J., Huang, M., Jin, H., 2011. Analysis of the formation of fog and haze in North China Plain (NCP). *Atmos. Chem. Phys.* 11, 8205–8214. <http://dx.doi.org/10.5194/acp-11-8205-2011>.
- Rahman, H., Pinty, B., Verstraete, M.M., 1993. Coupled surface-atmosphere reflectance (CSAR) model: 2. Semiempirical surface model usable with NOAA advanced very high resolution radiometer data. *J. Geophys. Res.-Atmos.* 98 (D11), 20,791–20,801. <http://dx.doi.org/10.1029/93JD02072>.
- Ramanathan, V., Crutzen, P.J., Kiehl, J.T., Rosenfeld, D., 2001. Aerosols, climate, and the hydrological cycle. *Science* 294, 2119–2124. <http://dx.doi.org/10.1126/science.1064034>.
- Ramanathan, V., Ramana, M.V., Roberts, G., Kim, D., Corrigan, C., Hung, C., Winker, D., 2007. Warming trends in Asia amplified by brown cloud solar absorption. *Nature* 448, 575–578. <http://dx.doi.org/10.1038/nature06019>.
- Remer, L.A., Kaufman, Y.J., Tanre, D., Mattoo, S., Chu, D.A., Martins, J.V., ... Holben, B.N., 2005. The MODIS aerosol algorithm, products, and validation. *J. Atmos. Sci.* 62, 947–973. <http://dx.doi.org/10.1175/JAS3385.1>.
- Rodriguez, E., Kolmonen, P., Virtanen, T.H., Sogacheva, L., Sundström, A.M., de Leeuw, G., 2015. Indirect estimation of absorption properties for fine aerosol particles using AATSR observations: a case study of wildfires in Russia in 2010. *Atmos. Meas. Tech.* 8 (8), 3075–3085. <http://dx.doi.org/10.5194/amt-8-3075-2015>.
- Russell, P.B., Bergstrom, R.W., Shinozuka, Y., Clarke, A.D., De-Carlo, P.F., Jimenez, J.L., ... Strawa, A., 2010. Absorption Ångström exponent in AERONET and related data as an indicator of aerosol composition. *Atmos. Chem. Phys.* 10, 1155–1169. <http://dx.doi.org/10.5194/acp-10-1155-2010>.
- Sayer, A.M., Hsu, N.C., Bettenhausen, C., Jeong, M.J., 2013. Validation and uncertainty estimates for MODIS Collection 6 “Deep Blue” aerosol data. *J. Geophys. Res.-Atmos.* 118 (14), 7864–7872. <http://dx.doi.org/10.1002/jgrd.50600>.
- Seidel, F.C., Kokhanovsky, A.A., Schaepman, M.E., 2010. Fast and simple model for atmospheric radiative transfer. *Atmos. Meas. Tech.* 3, 1129–1141.
- Seidel, F.C., Kokhanovsky, A.A., Schaepman, M.E., 2012. Fast retrieval of aerosol optical depth and its sensitivity to surface albedo using remote sensing data. *Atmos. Res.* 116 (8), 22–32. <http://dx.doi.org/10.1016/j.atmosres.2011.03.006>.
- Sekiyama, T.T., Yumimoto, K., Tanaka, T.Y., Nagao, T., Kikuchi, M., Murakami, H., 2016. Data assimilation of Himawari-8 aerosol observations: Asian dust forecast in June 2015. *Sci. Online Lett. Atmos.* 12, 86–90. <http://dx.doi.org/10.2151/sola.2016-020>.
- Smirnov, A., Holben, B.N., Eck, T.F., Dubovik, O., Slutsker, I., 2000. Cloud-screening and quality control algorithms for the AERONET database. *Remote Sens. Environ.* 73 (3), 337–349. [http://dx.doi.org/10.1016/S0034-4257\(00\)00109-7](http://dx.doi.org/10.1016/S0034-4257(00)00109-7).
- Soni, K., Singh, S., Bano, T., Tanwar, R.S., Nath, S., 2011. Wavelength dependence of the aerosol Ångström exponent and its implications over Delhi, India. *Aerosol Sci. Technol.* 45 (12), 1488–1498. <http://dx.doi.org/10.1080/02786826.2011.601774>.
- Sun, L., Wei, J., Bilal, M., Tian, X., Jia, C., Guo, Y., Mi, X., 2015. Aerosol optical depth retrieval over bright areas using Landsat 8 OLI images. *Remote Sens.* 8 (1), 23–36. <http://dx.doi.org/10.3390/rs8010023>.
- Sun, K., Chen, X., Wang, J., Zhang, T., Zhu, Z., 2017. Investigation of air quality over the largest city in central china using high resolution satellite derived aerosol optical depth data. *Atmos. Pollut. Res.* <http://dx.doi.org/10.1016/j.apr.2017.12.011>. (in press, corrected proof, Available online 29 December 2017).
- Tanre, D., Herman, M., Deschamps, P.Y., Lefé, A., 1979. Atmospheric modeling for space measurements of ground reflectances, including bidirectional properties. *Appl. Opt.* 18, 3587–3594. <http://dx.doi.org/10.1364/AO.18.003587>.
- Tao, M., Chen, L., Su, L., Tao, J., 2012. Satellite observation of regional haze pollution over the North China Plain. *J. Geophys. Res.-Atmos.* 117, D12203. <http://dx.doi.org/10.1029/2012JD017915>.
- Torres, O., Tanskanen, A., Veihelmann, B., Ahn, C., Braak, R., Bhartia, P.K., ... Levelt, P., 2007. Aerosols and surface UV products from Ozone Monitoring Instrument observations: an overview. *J. Geophys. Res.-Atmos.* 112 (D24), 1–14. <http://dx.doi.org/10.1029/2007JD008809>.
- Vermote, E.F., Tanré, D., Deuze, J.L., Herman, M., Morcrette, J.J., 1997. Second simulation of the satellite signal in the solar spectrum, 6S: an overview. *IEEE Trans. Geosci. Remote Sens.* 35, 675–686. <http://dx.doi.org/10.1109/36.581987>.
- Vermote, E.F., Tanré, D., Deuze, J.L., Herman, M., Morcrette, J.J., Kotchenova, S.Y., 2006. Second simulation of a satellite signal in the solar spectrum-vector (6SV). In: *6S User Guide Version. 3*. pp. 1–55.
- Wang, J., Xu, X.G., Spurr, R., Wang, Y., Drury, E., 2010. Improved algorithm for MODIS imagery over land surface. *Remote Sens. Environ.* 114, 2575–2583. <http://dx.doi.org/10.1016/j.rse.2010.05.034>.
- Wong, M.S., Nichol, J.E., Lee, K.H., 2011. An operational MODIS aerosol retrieval algorithm at high spatial resolution, and its application over a complex urban region. *Atmos. Res.* 99, 579–589. <http://dx.doi.org/10.1016/j.atmosres.2010.12.015>.
- Wu, Y., de Graaf, M., Menenti, M., 2016. Improved MODIS Dark Target aerosol optical depth algorithm over land: angular effect correction. *Atmos. Meas. Tech.* 9 (11), 5575–5589. <http://dx.doi.org/10.5194/amt-9-5575-2016>.
- Yan, X., Shi, W., Luo, N., Zhao, W., 2016. A new method of satellite-based haze aerosol monitoring over the North China Plain and a comparison with MODIS Collection 6 aerosol products. *Atmos. Res.* 171, 31–40. <http://dx.doi.org/10.1016/j.atmosres.2015.12.003>.
- Yan, X., Li, Z., Shi, W., Luo, N., Wu, T., Zhao, W., 2017. An improved algorithm for retrieving the fine-mode fraction of aerosol optical thickness, Part 1: algorithm development. *Remote Sens. Environ.* 192, 87–97. <http://dx.doi.org/10.1016/j.rse.2017.02.005>.
- Zaman, N., Kanniiah, K.D., Kaskaoutis, D.G., 2017. Estimating particulate matter using satellite based aerosol optical depth and meteorological variables in Malaysia. *Atmos. Res.* 193, 142–162.